



The Infrared Medium-deep Survey. III. Survey of Luminous Quasars at $4.7 \leq z \leq 5.4$

Yiseul Jeon^{1,2,10} , Myungshin Im^{1,10} , Dohyeong Kim¹, Yongjung Kim¹ , Hyunsung David Jun^{1,3,4} , Soojong Pak⁵ ,
Yoon Chan Taak¹, Giseon Baek⁵, Changsu Choi¹, Nahyun Choi⁶, Jueun Hong¹, Minhee Hyun¹, Tae-Geun Ji⁵,
Marios Karouzos^{1,7} , Duho Kim^{1,8} , Jae-Woo Kim^{1,9}, Ji Hoon Kim^{1,10} , Minjin Kim⁹ , Sanghyuk Kim⁹, Hye-In Lee⁵,
Seong-Kook Lee¹ , Won-Keek Park^{1,9}, Woojin Park⁵, and Yongmin Yoon¹

¹ Center for the Exploration of the Origin of the Universe (CEOU), Astronomy Program, Department of Physics & Astronomy, Seoul National University, 1 Gwanak-ro, Gwanak-gu, Seoul 151-742 Korea; ysjeon@astro.snu.ac.kr, mim@astro.snu.ac.kr

² LOCOOP, Inc., 311-1, 108 Gasandigital2-ro, Geumcheon-gu, Seoul, Korea

³ Jet Propulsion Laboratory, California Institute of Technology, 4800 Oak Grove Drive, Pasadena, CA 91109, USA

⁴ School of Physics, Korea Institute for Advanced Study, 85 Hoegiro, Dongdaemun-gu, Seoul 02455, Korea

⁵ School of Space Research, Kyung Hee University, 1732 Deogyong-daero, Giheung-gu, Yongin-si, Gyeonggi-do 446-701, Korea

⁶ SongAm Space Center, 103, 185 Gwonnyul-ro, Jangheung-myeon, Yangju-si, Gyeonggi-do 482-812 Korea

⁷ Astronomy Program, Department of Physics & Astronomy, Seoul National University, 1 Gwanak-ro, Gwanak-gu, Seoul 151-742 Korea

⁸ Arizona State University, School of Earth and Space Exploration, P.O. Box 871404, Tempe, AZ 85287-1404, USA

⁹ Korea Astronomy and Space Science Institute, 776 Daedeokdae-ro, Yuseong-gu, Daejeon, Korea

¹⁰ Subaru Telescope, National Astronomical Observatory of Japan, 650 North A'ohoku Place, Hilo, HI 96720, USA

Received 2016 November 14; revised 2017 June 1; accepted 2017 June 19; published 2017 August 4

Abstract

We present the first results of our survey for high-redshift quasars at $5 \lesssim z \lesssim 5.7$. The search for quasars in this redshift range has been known to be challenging due to the limitations of the filter sets used in previous studies. We conducted a quasar survey for two specific redshift ranges, $4.60 \leq z \leq 5.40$ and $5.50 \leq z \leq 6.05$, using multi-wavelength data that include observations made with custom-designed filters, *is* and *iz*. Using these filters and a new selection technique, we were able to reduce the fraction of interlopers. Through optical spectroscopy, we confirmed six quasars at $4.7 \leq z \leq 5.4$ with $-27.4 < M_{1450} < -26.4$ that recently were discovered independently by another group. We estimated black hole masses and Eddington ratios of four of these quasars from optical and near-infrared spectra, and found that these quasars are undergoing nearly Eddington-limited accretion that is consistent with the rapid growth of supermassive black holes in luminous quasars at $z \sim 5$.

Key words: cosmology: observations – quasars: emission lines – quasars: general – quasars: supermassive black holes – surveys

1. Introduction

Observations have shown that large numbers of quasars are found at $z \sim 4.5$ and at $z > 6$ (e.g., Fan et al. 2003, 2006; Willott et al. 2007, 2010b; Jiang et al. 2008, 2009, 2015; Mortlock et al. 2009, 2011; McGreer et al. 2013; Bañados et al. 2016). They harbor supermassive black holes (SMBHs) as massive as $\sim 10^{10} M_{\odot}$ (e.g., Jiang et al. 2007; Kurk et al. 2007; Jun et al. 2015; Wu et al. 2015), and appear to be vigorously evolving (Im 2009; Jiang et al. 2010; Shen et al. 2011; Jun et al. 2015). However, there is a dearth of quasars with measured black hole masses, which makes it difficult to investigate how they evolved at $5 < z < 6$ (e.g., Figure 16 in Jun et al. 2015). Measuring the black hole masses for a significant number of objects at this redshift range allows us to: (1) derive the Eddington luminosities, and consequently, the Eddington ratios, to understand the growth of these quasars (one simply expects the growth to slow down toward lower redshifts, in comparison to $z \sim 6$); (2) construct the black hole mass function to understand the cosmic emergence of the most massive quasars; (3) investigate the spectral energy distributions (SEDs) of quasars, to explore whether quasars with very massive black holes have a lower accretion-disk temperature (Laor & Davis 2011; Wang et al. 2014).

The redshift gap at $5 < z < 6$ mentioned above is partly due to the inefficiency of quasar selection techniques at $5.2 < z < 5.7$ in previous studies (e.g., Zheng et al. 2000; Schneider et al. 2001; Sharp et al. 2001; Fan et al. 2003, 2006; Mahabal et al. 2005; Cool et al. 2006; Willott et al. 2007, 2010b; Jiang et al. 2008, 2009, 2015; Wu & Jia 2010; Ikeda et al. 2012; Matute et al. 2013; McGreer et al. 2013). This low efficiency is due to limitations of current filter systems employed by these studies; the colors of $z \sim 5.5$ quasars using conventional filters are similar to those of late-type stars or brown dwarfs. Figure 1 shows two color–color diagrams generally used for high-redshift quasar selection. The black solid lines with asterisks are quasar tracks redshifted from the Sloan Digital Sky Survey (SDSS) composite quasar template of Vanden Berk et al. (2001), including the intergalactic medium (IGM) attenuation (Madau et al. 1996). The triangles are model colors of brown dwarfs from Burrows et al. (2006); the squares are model colors of stars from Hewett et al. (2006), out of the Bruzual–Persson–Gunn–Stryker (BPGS) atlas; and the crosses are point-like sources from the SDSS Star Catalog. Fan et al. (1999) used the $r-i$ versus $i-z$ color–color diagram to identify quasars at $z > 4.5$ (Figure 1(a): *r*-dropout quasars). Willott et al. (2009) used the $i-z$ versus $z-J$ color–color diagram for quasars at $z \sim 6$ (Figure 1(b): *i*-dropout quasars). The solid boxes indicate their quasar selection criteria. We see that *r*-dropout quasars at $z > 5.1$ (Figure 1(a)) and *i*-dropout quasars at $z < 5.7$ (Figure 1(b)) are mixed with the late-type stars or brown dwarfs on these color–color diagrams.

* Based on observations made with ESO Telescopes at the La Silla Paranal Observatory, under programme 091.A-0878.

¹⁰ Visiting Astronomer, Kitt Peak National Observatory, National Optical Astronomy Observatory, which is operated by the Association of Universities for Research in Astronomy, Inc. (AURA), under cooperative agreement with the National Science Foundation.

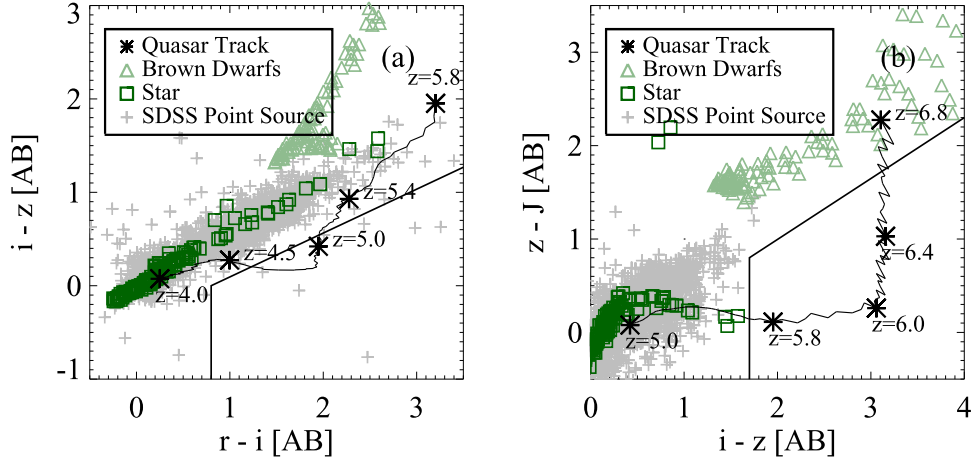


Figure 1. Color-color diagrams adopted by Fan et al. (1999) (left) and Willott et al. (2009) (right) for high-redshift quasar selection. The black solid lines with asterisks are quasar redshift tracks, the triangles are model colors of brown dwarfs, the squares are model colors of stars, and the crosses are point-like sources from the SDSS Star Catalog. The quasar tracks from $z = 5.1$ to $z = 5.7$ coincide with late-type stars or brown dwarfs. The solid boxes indicate the quasar selection boxes.

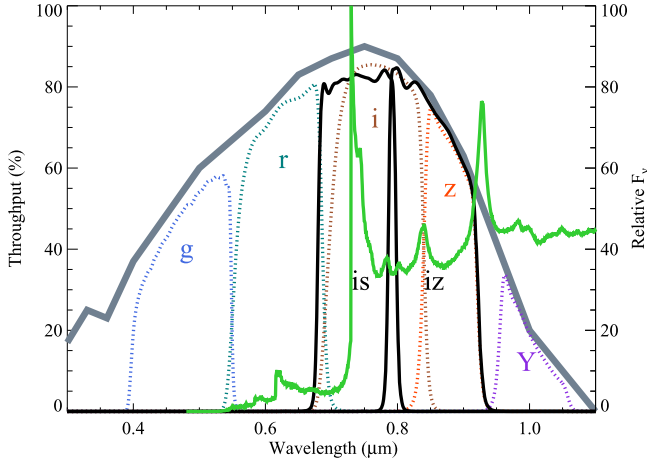


Figure 2. Filter transmission curves of is and iz (black solid lines), SDSS gri , and LSST zY bands (colored dashed lines), as well as the QE of the CCD (gray solid line) of CQUEAN. The green line represents the SDSS composite quasar spectrum from Vanden Berk et al. (2001) redshifted to $z = 5$, with IGM attenuation (Madau et al. 1996).

Therefore, the r -dropout technique alone cannot be used for $z \sim 5.5$ quasar selection. As can be seen from the above, any configuration of colors from SDSS $ugriz$ or the Two Micron All Sky Survey (2MASS) JHK filters cannot effectively separate quasars at $5.1 < z < 5.7$ from stars; a new filter system that exploits the wavelength range between conventional filters is necessary to find these quasars.

Thus, we searched for and studied high-redshift quasars at $5 < z < 6$ by using additional new data sets and performing follow-up observations. First, we designed a new filter set, is and iz , to supplement the previous filter systems for selecting quasars at this redshift range. Because the central wavelengths of these filters are located between r and i , and i and z , respectively, we can select high-redshift quasars at this redshift gap, where the SDSS or other filter sets cannot explore. Second, we needed a special optical detector that has better sensitivity than previous CCDs at longer wavelengths, leading to more efficient observations with the is and iz filters. Considering these requirements, we developed a CCD camera system, the Camera for QUasars in EARly uNiverse (CQUEAN; Kim et al. 2011; Park et al. 2012; Lim et al. 2013). Equipping a deep-depletion CCD chip to provide

high quantum efficiency (QE) at $0.7\text{--}1\ \mu\text{m}$, we conducted follow-up imaging observations of quasar candidates with the is and iz filters, then narrowed down the quasar candidates. CQUEAN was installed on the 2.1 m Otto Struve Telescope at McDonald Observatory in 2010 August, and it has since been used to obtain photometric data for many scientific programs, including our high-redshift quasar survey. In Figure 2, we plot the filter transmission curves of is and iz (black solid lines), the SDSS gri , and the Large Synoptic Survey Telescope zY bands (colored dashed lines) installed on CQUEAN, with the QE of the CCD taken into consideration (gray solid line). The green line represents the SDSS composite quasar template redshifted to $z \sim 5$, with IGM attenuation taken into consideration. Note that a similar survey of $z \sim 5$ luminous quasars is being conducted by Wang et al. (2016) and Yang et al. (2016). Their method relies on the archived multi-wavelength data set only, whereas our method includes the use of the custom is and iz filters.

Section 2 describes our quasar selection algorithm including color cuts, multi-wavelength data used, and imaging and spectroscopic follow-up observations. The photometric and spectroscopic analysis of our discovered quasars are shown in Section 3. We discuss our quasar selection efficiency and expected number of quasars in Section 4. Section 5 presents physical properties of the newly discovered quasars from the spectroscopy. Finally, we summarize this survey in Section 6. Throughout this paper, we use a cosmology with $\Omega_M = 0.3$, $\Omega_\Lambda = 0.7$ (e.g., Im et al. 1997), and $H_0 = 70\ \text{km s}^{-1}\ \text{Mpc}^{-1}$. We also use the AB magnitude system.

2. Quasar Selection and Observation

2.1. Quasar Candidate Selection

To select quasars at $5 < z < 6$, we employed multi-wavelength data that cover a large area: SDSS DR8, and the United Kingdom Infra-Red Telescope Infrared Deep Sky Survey Large Area Survey (UKIDSS LAS; Lawrence et al. 2007) DR10; the full overlapping area between the two surveys is $\sim 3400\ \text{deg}^2$. The r , i , z , J , and K magnitudes are used. Because the contamination rate using these filters is still high, we adopted is and iz -band photometry to discriminate brown dwarfs from r -dropout objects. We then set additional criteria to assign priorities for follow-up observations. No stellarity cut is made, to avoid missing quasars that are classified as extended objects (e.g., due to host galaxy or

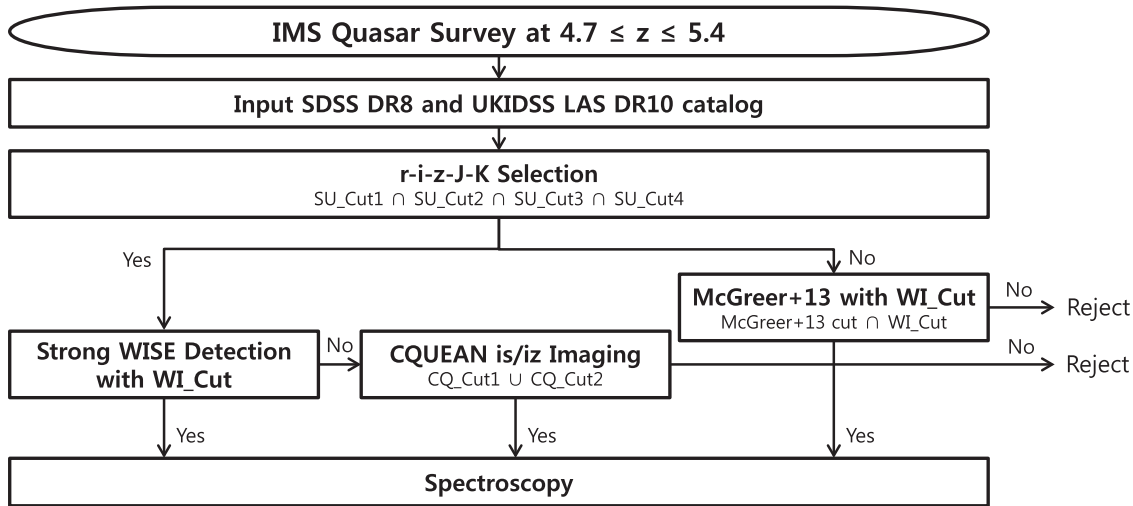


Figure 3. Schematic flow diagram of the main quasar candidate selection algorithm.

noise in stellarity calculation), although we used the stellarity as a way to set priorities for follow-up observation. Figure 3 shows a main quasar candidate selection algorithm.

2.1.1. $r-i-z-J-K$, is and iz -band Selections

To select quasar candidates from broadband photometry, we used the dropout feature at the $\text{Ly}\alpha$ emission line that is common in high-redshift objects. The $\text{Ly}\alpha$ dropouts can be identified using the $r-i$ color for quasars at $z > 3.6$, and $r-i > 1.5$ for quasars at $z > 4.6$. To discriminate high-redshift quasars from red, low-mass stars, we used three color cuts, $r-i$, $z-J$, and $J-K$: $r-i$ to select dropout objects, $z-J$ to remove brown dwarfs, and $J-K$ to eliminate other stars. Figure 4 shows two color-color diagrams with model brown dwarfs from Burrows et al. (2006) (green triangles), observed brown dwarfs from Patten et al. (2006) and Zhang et al. (2009) (green squares), and stellar sources from the SDSS catalog (gray circles, $\sim 10,000$ randomly selected sources). The black dots indicate SDSS stellar sources with $r-i > 1.5$. To verify the position of quasars at $4 < z < 6$, we plotted previously discovered quasars from the SDSS DR7 quasar catalog and Leipski et al. (2014) (crosses; the color indicates its redshift, as shown on the color bar in Figure 4(b)). The quasar redshift track at $4 < z < 6$ is plotted with the black solid line by assuming the redshifted and IGM-attenuated SDSS composite quasar template. The thick solid lines indicate the selection cuts for our quasar selection, and the dotted box in (a) is the selection box from Fan et al. (1999) for comparison. The selection boxes from SDSS and UKIDSS LAS data sets are defined as below:

$$\begin{aligned} \text{SU_Cut1)} & r-i > 1.5 \\ \text{SU_Cut2)} & [0 < J-K < 1] \cap [-1 < z-J < 0.5] \\ & \cap [(z-J) < (J-K) + 0.2] \end{aligned}$$

SU_Cut1 is for selecting the r -dropout objects and SU_Cut2 is for weeding out late-type stars and brown dwarfs. Because SU_Cut1 does not adopt the $i-z$ cut, unlike Fan et al. (1999), quasar candidates at $z \sim 5.5$ can be selected with this color cut. However, because the selection box of SU_Cut2 is close to the stellar locus (gray circles), and some of the stellar

sources selected from SU_Cut1 are still located inside SU_Cut2 (black circles inside SU_Cut2), the selected sample is still significantly contaminated by stars (more than 99% of the selected objects are expected to be stars; see Section 4.2).

To reduce stellar contamination in our sample, we impose magnitude cuts in the shorter wavelength data, as well as in the z -band. We set the magnitude cuts as below:

$$\begin{aligned} \text{SU_Cut3)} & u, g \text{ fainter than the } 3\sigma \\ & \text{detection limits } (u > 22.85 \text{ and} \\ & g > 23.55 \text{ mag}) \\ \text{SU_Cut4)} & z < 19.5 \text{ mag} \end{aligned}$$

From the cross-matched sources from SDSS DR8 and UKIDSS LAS DR10, 98.4% of sources are rejected via the above four criteria. After visual inspection for false detection, about 3600 candidates are finally listed. We checked the sources that were classified as quasars at $z > 4.6$ from the SDSS DR7 quasar catalog, and found that 14 quasars at $4.69 < z < 5.29$ and 2 quasars at $5.50 < z < 6.05$ were already spectroscopically identified. These ~ 3600 candidates still contain a significant fraction of contaminants, considering that the expected number of quasars at $z \sim 5$ in 3400 deg^2 is ~ 30 (Section 4.2), showing that about 99% of these sources will be interlopers. This is because the selected candidates from these two color-color diagrams are still contaminated by stellar sources, which are shown as the black circles inside SU_Cut2 in Figure 4(b). To eliminate these contaminants, we employed an additional selection method: photometry from is/iz -bands.

We now apply selection cuts, using the is and iz -bands of CQUEAN. The color cuts were defined using quasar redshift tracks. We optimized our quasar selection using CQ_Cut1 ($r-is-iz$: selection method A) or CQ_Cut2 ($is-iz-J$: selection method B) on color-color diagrams, which explore the redshift ranges of $4.60 \leq z \leq 5.40$ and $5.50 \leq z \leq 6.05$, respectively (Section 4.1). The criteria for the selections are:

$$\text{CQ_Cut1 } (r-is-iz \text{ for } 4.60 \leq z \leq 5.40): \\ \text{selection method A}$$

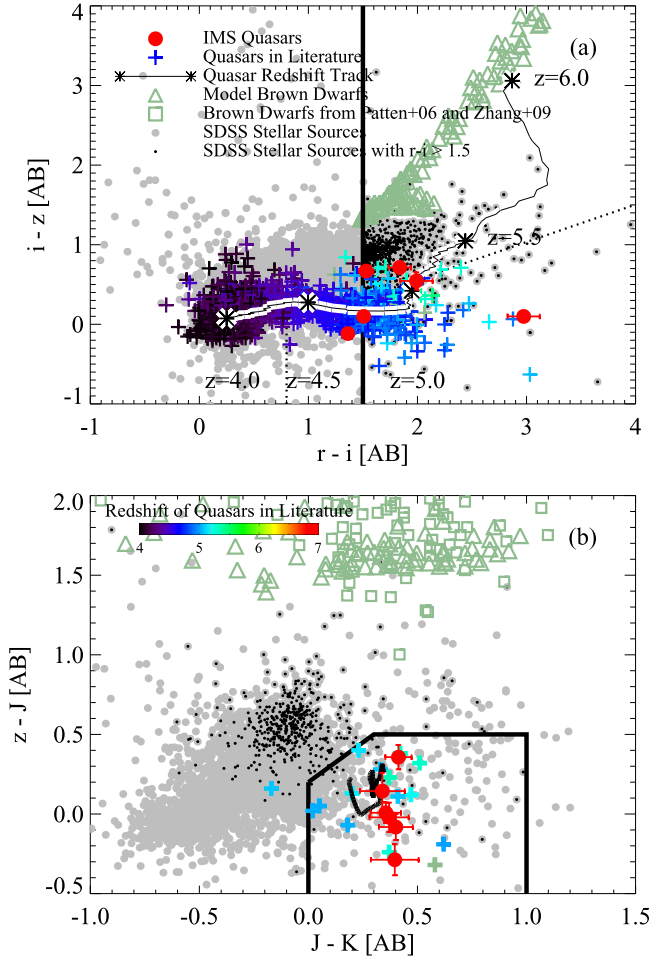


Figure 4. Two color-color diagrams we adopted for quasar selection at $5 \lesssim z \lesssim 5.7$. We plot the model brown dwarfs (green triangles), observed brown dwarfs from Patten et al. (2006) and Zhang et al. (2009) (green squares), stellar sources from SDSS (gray circles), previously discovered quasars (crosses), and the redshift tracks of quasars at $4 < z < 6$ (black solid line with asterisks in (a) and black solid line in (b)). Thick solid lines indicate the boxes for our quasar selection, and the dotted box in (a) is the selection box of Fan et al. (1999) for comparison. The black dots are SDSS stellar sources with $r - i > 1.5$; they show a high contamination rate even after the $z - J - K$ cut. We plotted our six new quasars with red circles (this work); most of them are within the selection boxes. One exception is IMS J0324+0426 in the $r - i - z$ color-color diagram, which was selected using the color cuts of McGreer et al. (2013).

$$\begin{aligned}
 & [r - is > 1.2] \cap [is - iz \\
 & < 1.2] \cap [is - iz \\
 & < 1.5 \times (r - is) - 1.2] \\
 & \text{CQ_Cut2 } (is - iz - J \text{ for } 5.50 \leq z \leq 6.05): \\
 & \text{selection method B} \\
 & [s - iz > 1.8] \cap [iz - J < 1.5].
 \end{aligned}$$

Figure 5 shows these two color-color diagrams with quasar redshift tracks (black lines with asterisks from the redshifted and IGM-attenuated SDSS composite quasar template), model brown dwarfs (green triangles; from Burrows et al. 2006), stars from Gunn & Stryker (1983) (green squares), star-forming galaxy redshift tracks (blue line; model colors from M51),

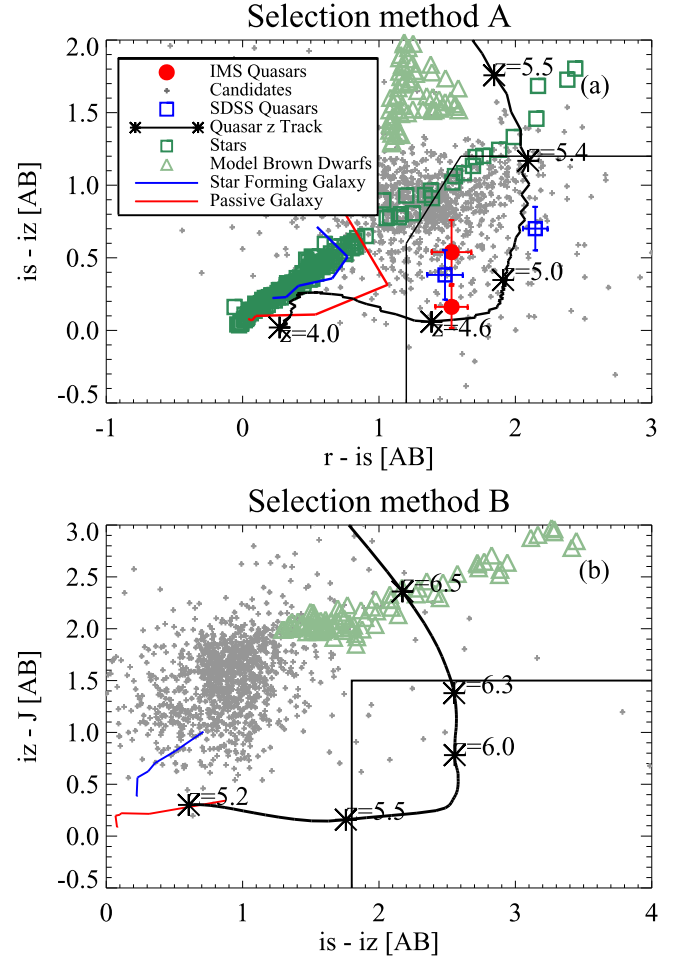


Figure 5. Two color-color diagrams using is and iz -bands. Quasar candidates (gray crosses), SDSS quasars (blue squares), quasar redshift tracks (black lines with asterisks), model brown dwarfs (green triangles), stars (green squares), star-forming galaxy redshift tracks (blue lines), passive galaxy redshift tracks (red lines), and the two selection boxes are plotted. We plotted our two new quasars with the is and iz photometry as red circles in (a).

passive galaxy redshift tracks (red line; model colors from the Bruzual & Charlot (2003), a model of a passively evolving, 5 Gyr-old galaxy with spontaneous burst, metallicity of $Z = 0.02$, and the Salpeter initial mass function), and SDSS quasars with is and iz observations, for comparison (blue square). The two color cuts are denoted. About 1400 of the ~ 3600 quasar candidates were imaged with CQUEAN (gray crosses); among them, about 500 candidates satisfy these color cuts. However, selected candidates in CQ_Cut1 still show a high contamination rate because the stellar locus is found near the quasar redshift track. After considering the spectral shape of quasars, we selected about 60 targets as promising candidates via visual inspection of SEDs, because quasars at $5 < z < 6$ tend to have $H - K$ colors redder than those of dwarf stars ($H - K \gtrsim 0$), due to the power-law continuum of quasars. During the visual inspection, SEDs that show a downturn in flux toward longer wavelengths (Figure 6(a)) are rejected in favor of those that are retained as candidates (Figure 6(b)).

2.1.2. Ancillary Selection

We set additional selection criteria for assigning priorities for imaging and spectroscopic follow-up observations.

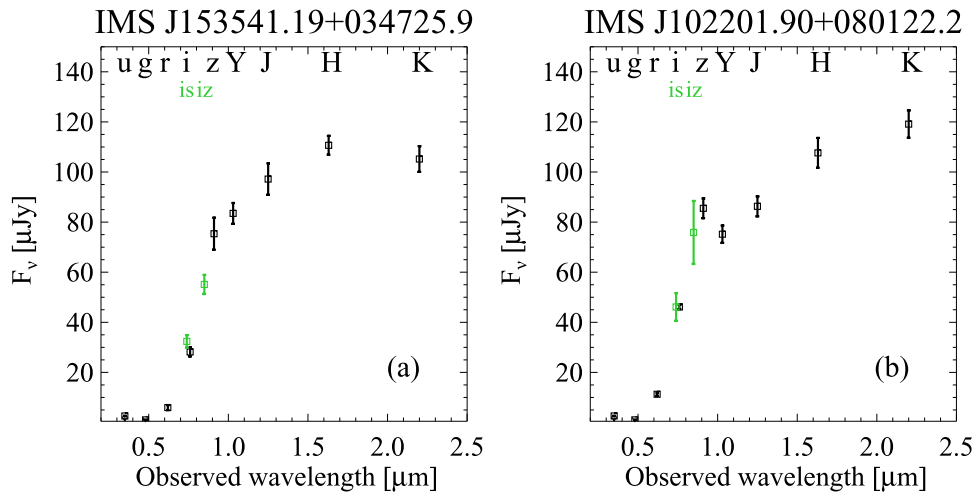


Figure 6. Examples of SEDs of u , g , r , is , i , iz , z , Y , J , H , and K -bands. The filter names are marked at each wavelength. The is and iz filters are plotted with green points. (a) shows a candidate with a blue $H - K$ color ($H - K = -0.06$) that is rejected after the visual inspection; (b) shows a candidate that turned out to be a high-redshift quasar ($H - K = 0.11$).

WISE Selection: The *WISE* catalog provides 3.4, 4.6, and 12 micron data ($W1$, $W2$, and $W3$ -bands) that are useful for quasar candidate selection. Due to the nature of quasar continua, we expect quasars at $z \sim 5$ to have $-0.6 < K - W1 < 2.0$ and $W1 - W2 > -0.6$, whereas about 60% of brown dwarfs do not. The cut of $W1 - W3 > -0.6$ is also adopted to remove the brown dwarf outliers, although this cut is not as powerful as the other *WISE* cuts. We selected red sources in *WISE* bands and assigned high priorities to these sources for follow-up observations. Figure 7 shows our ~ 3600 candidates with *WISE* detections (gray crosses), nine previously discovered quasars with *WISE* detections (blue squares), and model brown dwarfs (green triangles). Because the model brown dwarf templates from Burrows et al. (2006) do not extend to the $W3$ -band, only Figure 7(a) shows the colors of model brown dwarfs (green triangles). We do not consider the quasar redshift track because the rest-frame optical region of the quasar template from Vanden Berk et al. (2001), which is sampled by *WISE* bands, is affected by host galaxy. Therefore, based on the observed quasar colors, we defined WI_Cut (purple boxes). We adopt the following selections:

$$\begin{aligned} WI_Cut: & [W1 - W2 > -0.6] \\ & \cap [-0.6 < K - W1 < 2] \\ & \text{and/or } [W1 - W3 > -0.6] \\ & \cap [-0.6 < K - W1 < 2]. \end{aligned}$$

Candidates detected in *WISE* bands were assigned higher priorities. Some of them showed strong power-law continuum at the rest-frame ultraviolet spectral region, and thus were followed up with optical spectroscopy. Fifty three candidates were given higher priorities due to the *WISE* criteria (see Table 1).

Color cuts from McGreer et al. (2013): they discovered a number of quasars at $4.7 < z < 5.1$ over the area covered by SDSS, including Stripe 82. From the cross-matched sources of SDSS DR8 and UKIDSS LAS DR10, 148 candidates with $z < 19.5$ mag satisfy the these conditions, and nine of which are included in our ~ 3600 quasar candidates. We gave high priorities to candidates that satisfied the color cuts used in their work. Sources selected from these color cuts with *WISE*

selection, but not included in the $r - i - z - J - K$ color cuts, are also added to our candidate list.

Candidates from Polsterer et al. (2013): they provide a quasar candidate catalog containing 121,909 sources with photometric redshifts at $2.558 \leq z \leq 6.131$. Ten sources are included in our candidate list—we gave higher priorities to these sources.

Stellarity: we use `mergedClass` for UKIDSS LAS and `type` for SDSS to distinguish point sources from extended sources. We defined a source with `mergedClass = -1` or `-2`, or `type = 6`, as a point source, and gave higher priorities to these sources. We did not exclude the extended sources, because 17% of the discovered quasars from McGreer et al. (2013) are classified as extended sources in their i -band, meaning that some quasars may be classified as extended sources due to noise in the stellarity measurements or host galaxy contribution.

2.1.3. Selection Summary

The selection method used in this paper can be summarized as follows. We begin with an adjoint sample of SDSS DR8 and UKIDSS LAS DR10. We select objects showing Ly α drops between r and i , then remove brown dwarfs and stars using the $r - i - z - J - K$ color-color diagrams ($SU_Cut1, 2$). To decrease the number of stellar contaminants, we adopt magnitude cuts in the u , g , and z bands ($SU_Cut3, 4$). These four criteria decrease the sample to ~ 3600 objects. Among them, sources with strong *WISE* detection and *WISE* selection (WI_Cut) are listed as promising candidates. Objects not included in the $r - i - z - J - K$ selection, but selected from the McGreer et al. (2013) cuts with *WISE* selection (WI_Cut), are added to the candidate list. Among the ~ 3600 candidates, to reduce contamination, we utilized two color-color diagrams, $r - is - iz$ and $is - iz - J$, employing our new filter system and selected quasar candidates at two redshift ranges ($CQ_Cut1, 2$). For the CQUEAN imaging follow-up observations, we set priorities of our candidates considering the stellarity, *WISE* detection, color cuts from McGreer et al. (2013), and candidates from Polsterer et al. (2013). Objects showing point-like shapes with *WISE* detections, as well as satisfying the color cuts from McGreer et al. (2013) or

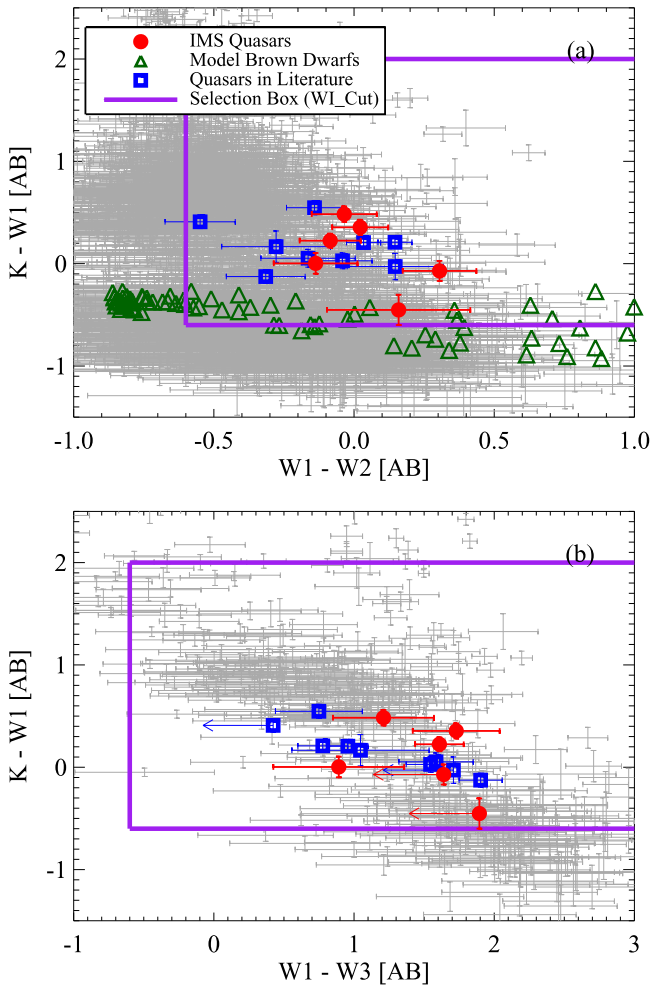


Figure 7. Two color-color diagrams with *WISE* photometry and our selection boxes. We plot our ~ 3600 candidates with *WISE* detections (gray crosses), previously known $z \sim 5$ quasars (blue squares), and model brown dwarfs (green triangles). We plotted our six new quasars as red circles.

Table 1
Priorities for CQUEAN Imaging Follow-up Observations

Priority	Stellarity	<i>WISE</i>	McGreer+13 or Polsterer+13	Number
0	yes	yes	yes	8
1	yes	no	yes	24
2	yes	yes	no	45
3	yes	no	no	1039
4		yes or yes or yes		1142
5	no		yes	123
10			others	1105

candidate list from Polsterer et al. (2013), were classified as important candidates. Table 1 lists the priority for each case, with smaller numbers indicating higher priorities. We have been conducting *is* and *iz* imaging for the high-priority objects, and about half of the sample was imaged in these two filters. Finally, via visual inspection of the SEDs, ~ 60 targets were selected to be our main samples for spectroscopy.

2.2. Optical Imaging Follow-up Observations with CQUEAN

Follow-up observations of our high redshift quasar candidates using CQUEAN began in 2010 August and are still

ongoing. About 1400 among ~ 3600 candidates with high priorities have been observed with CQUEAN to date.

We used short single exposure times of 30 and 60 s for the *iz* and *is* filters, respectively. Number of frames varied depending on the sky conditions, such as seeing conditions and extinction. If the peak value of a target was greater than 80 ADU after a 30 s exposure with *iz*, 2.5 (30 s \times 5) and 5 (60 s \times 5) minutes were used as the integration times for the *iz* and *is* filters, respectively. If the signal was lower than the criterion, we exposed for 5 (30 s \times 10) and 10 (60 s \times 10) minutes (or more) with *iz* and *is*, respectively.

Preprocessing, including bias subtraction, dark subtraction, and flat fielding, were performed using the usual data reduction procedures in the IRAF¹¹ `noao.imred.ccdred` package. Because the bias values may change with time (Park et al. 2012), we used bias images that were taken closest to the object frames, time-wise. We combined and averaged images of each field and filter. We used the `ccmap` task of IRAF and SCAMP (Bertin 2006) to derive astrometric solutions. SExtractor (Bertin & Arnouts 1996) was used for the source detection and photometry. We derived auto-magnitudes that are taken as the total magnitudes.

For the photometric calibration, we used SDSS photometry of stellar objects inside each target field. We performed χ^2 fitting to the SDSS *r*, *i*, and *z* magnitudes of stellar sources, to determine best-fit stellar spectral types. For this, we used the SED templates from Gunn & Stryker (1983), containing 175 spectra of various stellar types. The model *is* and *iz* magnitudes were calculated from the best-fit templates, and these are used to define the zero-points (Z_p) of each filter image of each field. The Z_p values were calculated for each star, and we took the average of these values as Z_p , and the standard deviation of the scatters as its Z_p error. The average Z_p error is about 0.05 mag. During the calculation, objects with large reduced χ^2 values ($\chi^2_\nu > 5$) were rejected for the estimation. Note that this photometric calibration method is described in more detail in Jeon et al. (2016).

2.3. Optical Spectroscopic Follow-up Observations

We observed 47 candidates using the Kitt Peak National Observatory (KPNO) 4 m Mayall telescope and the European Southern Observatory (ESO) New Technology Telescope (NTT). The KPNO 4 m observations were performed over three runs for 10 nights from 2013 January to September, and the NTT observation was done for three nights in 2013 May.

For the observations at KPNO, we used the Ritchey-Chrétien Focus Spectrograph in a longslit mode (RCSPL¹²), with an LB1A CCD, the BL400 grating of $R \sim 500$ for a 2'' slit, and OG400 filter. LB1A uses a thick CCD chip, and therefore does not suffer much from fringing. The wavelength coverage is 5000–10000 Å. For the observation at the ESO NTT, we used the ESO Faint Object Spectrograph and Camera v.2 (EFOSC2; Buzzoni et al. 1984). The EFOSC2 was used with Gr#2, which has a wavelength coverage of 5100–11000 Å and $R \sim 135$ for a 1'' slit. We took calibration frames including bias, dark, flat, and arc. Standard stars, such as G191B2B, GD153, CD-32d9927, LTT7379, LTT3864, Feige110, and HR7596 were

¹¹ IRAF is distributed by the National Optical Astronomy Observatory, which is operated by the Association of Universities for Research in Astronomy, Inc., under cooperative agreement with the National Science Foundation.

¹² <http://www-kpno.kpno.noao.edu/manuals/l2mspect/index.html>

Table 2
Spectroscopic Observation Summary of IMS Quasars

Spectroscopy	Date	Telescope	Target	Integration Time (minutes)	Slit Width (")
Optical	2013 Jan 16	KPNO 4 m	IMS J1022+0801	80	3.0
	2013 May 6	NTT	IMS J1437+0708	40	1.2
	2013 May 6	NTT	IMS J2225+0330	90	1.0
	2013 May 7	NTT	IMS J1437+0708	60	1.0
	2013 Sep 27	KPNO 4 m	IMS J0122+1216	45	1.5
	2013 Sep 28	KPNO 4 m	IMS J0155+0415	60	1.5
	2013 Sep 28	KPNO 4 m	IMS J0324+0426	45	1.5
	2013 Sep 29	KPNO 4 m	IMS J2225+0330	60	1.5
	2013 Sep 29	KPNO 4 m	IMS J0122+1216	45	1.5
NIR	2014 Oct 6	<i>Magellan</i>	IMS J0122+1216	60	1.0
	2014 Oct 7	<i>Magellan</i>	IMS J0155+0415	30	1.0
	2014 Oct 6	<i>Magellan</i>	IMS J0324+0426	60	1.0
	2015 Aug 30	Gemini-N	IMS J2225+0330	53	0.675

Table 3
General Information of IMS Quasars

Name	R.A. and Decl. (J2000.0)	Redshift	M_{1450}
IMS J032407.70+042613.3	03:24:07.70 + 04:26:13.3	4.70(Ly α) ^a , 4.68(C IV), 4.73(Mg II)	-27.21 ± 0.29
IMS J012247.33+121623.9	01:22:47.33 + 12:16:23.9	4.83(Ly α) ^b , 4.81(C IV)	-26.47 ± 0.68
IMS J143704.82+070808.3	14:37:04.82 + 07:08:08.3	4.94(Ly α) ^c	-27.14 ± 0.09
IMS J222514.39+033012.6	22:25:14.39 + 03:30:12.6	5.35(Ly α) ^d , 5.26(Mg II)	-26.47 ± 0.29
IMS J102201.90+080122.2	10:22:01.90 + 08:01:22.2	5.36(Ly α)	-27.38 ± 0.10
IMS J015533.28+041506.8	01:55:33.28 + 04:15:06.8	5.35(Ly α) ^e , 5.27(C IV)	-26.85 ± 1.09

Notes. z_{spec} from other papers are all derived from Ly α .

^a $z_{\text{spec}} = 4.72$ from Wang et al. (2016).

^b $z_{\text{spec}} = 4.76$ from Yi et al. (2015) and $z_{\text{spec}} = 4.79$ from Wang et al. (2016).

^c $z_{\text{spec}} = 4.93$ from Wang et al. (2016).

^d $z_{\text{spec}} = 5.24$ from Wang et al. (2016).

^e $z_{\text{spec}} = 5.37$ from Wang et al. (2016).

observed for the flux calibration. The slit widths varied from 1"0 to 3"0, depending on the seeing conditions. Table 2 shows the summary of the optical spectroscopic observations of the discovered quasars, namely the total integration time and the slit width for each target.

We followed the typical steps for preprocessing, including bias subtraction, dark subtraction, and flat fielding, for each science image, standard star image, and arc image, using the `noao.imred.ccdred` package in IRAF. The spectra were extracted using the `noao.imred.kpnoslit` or the `noao.twospec.apextract` packages in IRAF for each single image. We used an optimal aperture size for each image where the S/N is highest. After this, wavelength and flux calibrations were conducted. The spectra were flux-calibrated using spectra of the standard stars. Considering the light loss due to variable seeing conditions, we scaled the spectra using broadband photometry. We chose *i*-band for this calibration because we get the highest S/N in this band for the observed spectra. The flux-calibrated spectra were combined in median, using the `scombine` task of IRAF, then corrected for Galactic extinction using values from Cardelli et al. (1989) and Schlegel et al. (1998).

We observed 47 candidates, six of which turned out to be high-redshift quasars at $4.7 \leq z \leq 5.4$, referred to as Infrared Medium-deep Survey (IMS) quasars. Table 3 lists the names, coordinates, and redshifts (Section 3.2) of the six quasars. The naming

convention of our quasars is IMS JHHMMSS.SS \pm DDMMSS.S in J2000.0 coordinates (IMS JHHMM \pm DDMM for brevity).

2.4. NIR Spectroscopic Observation

To measure their black hole masses and Eddington ratios, we observed four of the six newly discovered quasars with the Folded-port InfraRed Echellette (FIRE¹³) spectrograph on the *Magellan* telescope (IMS J0324+0426, IMS J0122+1216, and IMS J0155+0415), as well as with the Gemini Near Infra-Red Spectrograph (GNIRS) on the Gemini North (Gemini-N) telescope (IMS J2225+0330; program GN-2015B-Q-77). Table 2 shows the summary of our *Magellan* and Gemini-N observations.

In the *Magellan*/FIRE observation, we used a slit width of 1"00 with the Echelle mode ($R = 3600$). The ABBA pointing method was used for the sky subtraction between exposures. We observed standard stars for each target. Data for the flat fielding and wavelength calibration were also taken. The data reduction was conducted using the IDL suite FIREHOSE. This pipeline conducts the preprocessing, object extraction, telluric correction, flux calibration, and spectra combining.

In the Gemini-N/GNIRS observation, we used the cross-dispersed (XD) mode with a 32 line mm^{-1} grating, short blue camera, and its SXD prism. Adopting a slit of 0"675 width, we

¹³ <http://web.mit.edu/~rsimcoe/www/FIRE/index.html>

Table 4
Optical Photometric Information for IMS Quasars

Name	g	r	i	z	is	iz
IMS J0324+0426	23.95 ± 0.39	20.39 ± 0.04	19.03 ± 0.03	19.15 ± 0.06
IMS J0122+1216	24.29 ± 0.37	22.35 ± 0.14	19.37 ± 0.03	19.27 ± 0.06
IMS J1437+0708	25.02 ± 0.72	20.71 ± 0.04	19.20 ± 0.02	19.10 ± 0.06	19.17 ± 0.11	19.01 ± 0.09
IMS J2225+0330	25.67 ± 0.68	22.01 ± 0.14	20.02 ± 0.05	19.47 ± 0.10
IMS J1022+0801	25.23 ± 0.64	21.27 ± 0.06	19.74 ± 0.02	19.07 ± 0.05	19.74 ± 0.13	19.20 ± 0.18
IMS J0155+0415	24.07 ± 0.38	21.81 ± 0.10	19.98 ± 0.03	19.26 ± 0.06

Table 5
NIR Photometric Information for IMS Quasars

Name	$W1$	$W2$	$W3$	$W4$	Y	J	H	K
IMS J0324+0426	18.47 ± 0.05	18.45 ± 0.09	16.74 ± 0.31	15.27 ± 0.38	19.39 ± 0.05	19.23 ± 0.05	18.96 ± 0.05	18.83 ± 0.05
IMS J0122+1216	18.28 ± 0.05	18.36 ± 0.09	16.67 ± 0.17	99.00 ± 99.00	19.12 ± 0.04	18.92 ± 0.04	18.56 ± 0.04	18.50 ± 0.04
IMS J1437+0708	18.99 ± 0.07	19.12 ± 0.13	18.10 ± 0.46	99.00 ± 99.00	19.40 ± 0.05	19.39 ± 0.08	19.01 ± 0.06	18.99 ± 0.08
IMS J2225+0330	19.44 ± 0.12	19.28 ± 0.22	99.00 ± 99.00	99.00 ± 99.00	19.48 ± 0.06	19.33 ± 0.06	19.04 ± 0.10	18.99 ± 0.08
IMS J1022+0801	18.23 ± 0.05	18.26 ± 0.10	17.01 ± 0.36	99.00 ± 99.00	19.21 ± 0.05	19.06 ± 0.05	18.82 ± 0.06	18.71 ± 0.05
IMS J0155+0415	18.98 ± 0.08	18.68 ± 0.11	99.00 ± 99.00	99.00 ± 99.00	19.66 ± 0.07	19.28 ± 0.06	19.00 ± 0.06	18.91 ± 0.06

Note. We used a dummy value of 99.99 for non-detections.

Table 6
Selection Methods of IMS Quasars

Name	$WISE^a$ ($K - W1 - W2$)	$WISE^b$ ($K - W1 - W3$)	McGreer+13 ^c	Polsterer+13 ^d	$r - is - iz^e$	$is - iz - J^f$
IMS J0324+0426	yes	yes	yes	no
IMS J0122+1216	yes	yes	yes	no
IMS J1437+0708	yes	yes	yes	yes	yes	...
IMS J2225+0330	yes	yes	no	no
IMS J1022+0801	yes	yes	no	no	yes	...
IMS J0155+0415	yes	yes	no	no

Notes.

^a Does it satisfy the color cut of $K - W1 - W2$?

^b Does it satisfy the color cut of $K - W1 - W3$?

^c Does it satisfy the color cuts from McGreer et al. (2013)?

^d Is it contained in the candidate list from Polsterer et al. (2013)?

^e Does it satisfy the color cut of $r - is - iz$?

^f Does it satisfy the color cut of $is - iz - J$?

obtained $R \sim 800$. We also used the ABBA pointing method, and observed standard stars and calibration data. For the data reduction, we used the Gemini IRAF package following the reduction scripts in the Gemini web page.¹⁴ The steps include pattern noise cleaning using the `clearnir` script, reducing the science data using flatfield images, combining images, wavelength calibration, extracting spectra, and flux calibration using standard stars.

We scaled the flux of the combined spectra using broadband photometry. After that, the spectra were corrected for Galactic extinction using Cardelli et al. (1989) and Schlegel et al. (1998).

3. High Redshift Quasars

3.1. Photometric Properties

Tables 4 and 5 list the photometric information for our newly discovered quasars from SDSS, UKIDSS LAS, *WISE*, and

CQUEAN. Table 6 shows their selection properties. All six of them have *WISE* detections and are located inside the *WISE* color cuts (Figure 7; $K - W1 - W2$ or $K - W1 - W3$). IMS J0324+0426, IMS J0122+1216, and IMS J1437+0708 also satisfy the color cuts of McGreer et al. (2013) that are aimed at selecting $z < 5.1$ quasars. Polsterer et al. (2013) provided a photometric redshift for IMS J1437+0708 of $z = 4.961 \pm 0.127$, which is in agreement with our redshift measured from the Ly α emission line (Section 3.2). For the two IMS quasars with *is* and *iz* photometry, Figure 5(a) shows their colors in the $r - is - iz$ color-color diagram.

Only two quasars among ~ 1400 sources with *is* and *iz* photometry were newly identified as high-redshift quasars in the $r - is - iz$ color-color diagram, and none of our candidates were discovered in the $is - iz - J$ color-color diagram. The other quasars were selected as candidates using the *WISE* photometry or the color cuts from McGreer et al. (2013). The expected numbers of quasars for each selection method from 3400 deg^2 are $24.4^{+67.7}_{-17.9}$ for $4.60 \leq z \leq 5.40$, and $5.6^{+15.4}_{-4.1}$ for $5.50 \leq z \leq 6.05$ (Section 4.2). For $4.60 \leq z \leq 5.40$, the six quasars were found. Including 14 previously discovered

¹⁴ <https://www.gemini.edu/sciops/instruments/gnirs/data-format-and-reduction/reducing-xd-spectra>

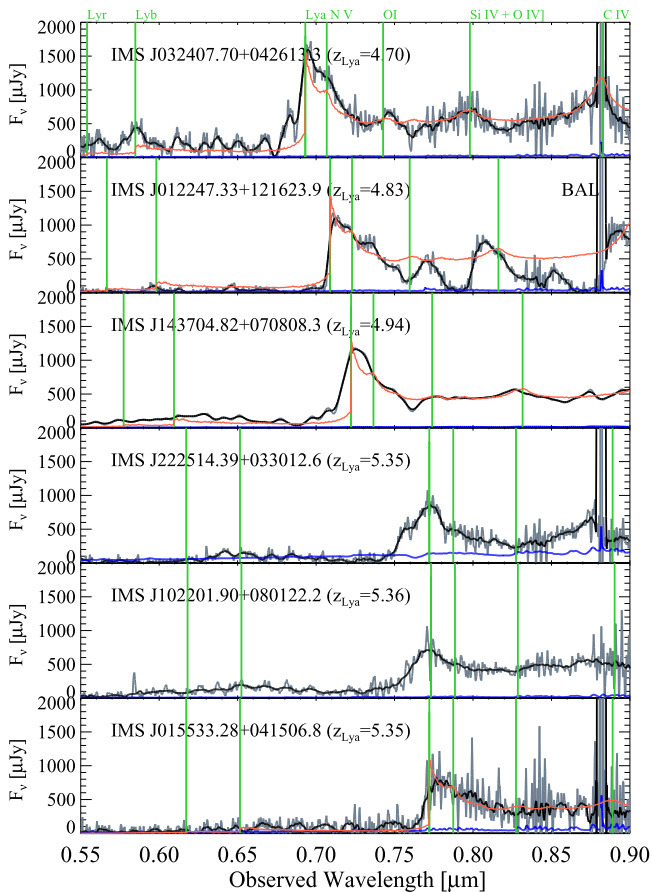


Figure 8. Optical spectra of the six quasars at $4.7 < z < 5.4$ from KPNO 4 m telescope/RCSPL and NTT/EFOCS2. The gray lines are the original (oversampled) spectra and the black lines are spectra smoothed to their respective instrumental resolution. The blue lines denote the errors of each spectrum. The orange line represents the redshifted composite spectrum of SDSS quasars (Vanden Berk et al. 2001), with the IGM attenuation included (Madau et al. 1996) and fit to the observed spectrum. The green lines indicate general quasar emission lines.

quasars in the literature brings the total number of quasars to 20, which agrees with the expected number. The selection for $5.50 \leq z \leq 6.05$ identified two quasars that were published in previous studies. Although we were unable to discover new quasars (see Section 4.2), this number is also as expected.

3.2. Spectroscopic Properties

First, we present the optical spectra of the six quasars at $4.7 \leq z \leq 5.4$ in Figure 8. We plotted spectra smoothed to the resolution of each instrument (black lines), together with the original spectra (gray lines). The blue lines denote the errors of the spectra.

Second, we present NIR spectra of four objects, IMS J0324+0426, IMS J0122+1216, IMS J2225+0330, and IMS J0155+0415 in Figure 9. The reduced spectra were binned to the spectral resolution of each instrument using the median statistics. Errors of the smoothed spectra were calculated from the errors of the original spectra via standard error propagation. For the spectrum from Gemini-N/GNIRS, the gray bars show regions of strong atmospheric absorption where the spectra shows low S/N.

We find diverse $\text{Ly}\alpha$ shapes for the six quasars. IMS J0324+0426, IMS J0122+1216, and IMS J1437+0708 show strong

$\text{Ly}\alpha$ emission, whereas the other three show smoother shapes. These weak $\text{Ly}\alpha$ lines are fairly common at high redshift. Jiang et al. (2009) and Bañados et al. (2014) show that a significant fraction of quasars at high redshift have weak $\text{Ly}\alpha$ (e.g., 25% of $z \sim 6$ quasars discovered by Bañados et al. 2014). Most of the emission lines, with the exception of $\text{Ly}\alpha$, are difficult to verify due to the imperfect sky line subtraction and low QE of the detector at wavelengths longer than $0.8 \mu\text{m}$. IMS J0122+1216 shows significant deep absorption features, and we classify it as a broad absorption line (BAL) quasar. This property can be noticed more clearly in its NIR spectrum.

Table 3 lists the redshifts and absolute magnitudes of the continua at rest-frame 1450 \AA (M_{1450}) of the quasars. The redshifts of IMS J2225+0330 and IMS J1022+0801 were measured from the $\text{Ly}\alpha$ emission lines by fitting Gaussian profiles. However, other spectra show a sharp blueward drop of $\text{Ly}\alpha$. In these cases, their redshifts were measured by fitting the spectra (the orange line in Figure 8) from the redshifted and IGM-attenuated SDSS composite quasar template. The redshift errors estimated from these optical spectra contain the uncertainties from the spectral resolution of each instrument (typically ~ 0.05), because one of the most dominant uncertainties of the redshift measurement is caused by the low spectral resolution. We also list the redshifts estimated using the C IV or Mg II emission lines from the NIR spectra (see Section 5) in Table 3. The redshift error estimated from the NIR spectra due to the spectral resolution is about 0.002 for *Magellan*/FIRE and about 0.007 for Gemini-N/GNIRS. The redshifts estimated from the optical and NIR spectra show discrepancies that we believe are caused by the ambiguous $\text{Ly}\alpha$ shapes, which can be heavily affected by the $\text{Ly}\alpha$ forest and blending with the NV emission line.

Richards et al. (2009, 2015) provide photometric redshifts (z_{phot}) for three out of the six quasars: IMS J0122+1216, IMS J1437+0708, and IMS J2225+0330. Their estimate for IMS J0122+1216 ($z_{\text{phot}} = 5.455^{+0.135}_{-0.095}$ from Richards et al. 2015) does not agree with our spectroscopic redshift ($z_{\text{Ly}\alpha} = 4.83$), but IMS J1437+0708 ($z_{\text{phot}} = 5.075^{+0.505}_{-0.455}$ from Richards et al. 2009 or $5.265^{+0.115}_{-0.505}$ from Richards et al. 2015) and IMS J2225+0330 ($z_{\text{phot}} = 5.415^{+0.285}_{-0.395}$ from Richards et al. 2015) are in agreement with our estimates ($z_{\text{Ly}\alpha} = 4.94$ and 5.35, respectively). The discrepancy between z_{phot} and z_{spec} for IMS J0122+1216 is likely because the object is a BAL quasar.

We calculated the M_{1450} values using the average flux at $1440\text{--}1460 \text{ \AA}$ from the optical spectra in Table 3. The uncertainties were estimated from the rms continuum flux density. For $z = 5.0$ quasars, the observed wavelength of the rest-frame 1450 \AA is located at 8700 \AA , where the sky emission lines are significant. Due to the difficulty of subtracting the sky from the relatively low S/N spectra, these values are crude and the actual magnitude uncertainties could be higher than our error estimates. Our IMS quasars are within the M_{1450} range of -27.4 to -26.4 .

3.3. Individual Properties of Quasars

IMS J0324+0426 ($z_{\text{Ly}\alpha} = 4.70$, $z_{\text{C IV}} = 4.68$, $z_{\text{Mg II}} = 4.73$). This quasar has a strong $\text{Ly}\alpha$ emission line. It also shows relatively strong $\text{Ly}\beta$, O I, Si IV+O IV, and C IV emission lines, as well as a weak NV emission line. In the NIR spectrum, C IV, C III], and Mg II emission lines are prominent. Wang et al. (2016) reported $z = 4.72$.

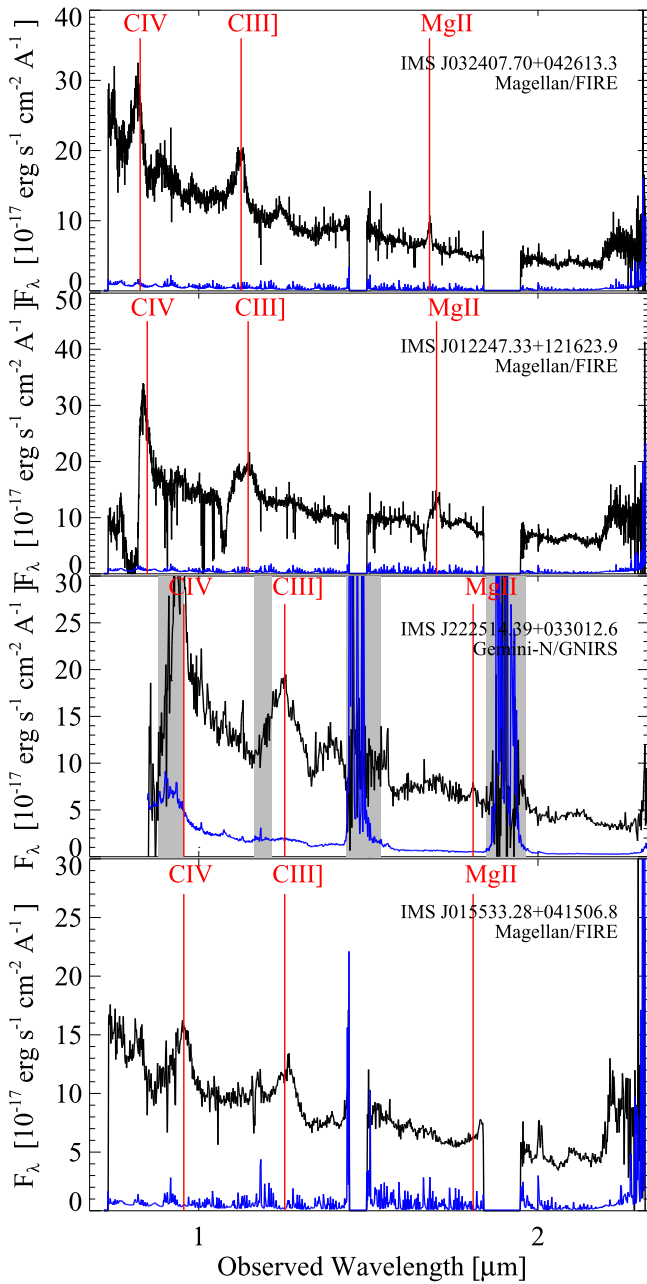


Figure 9. NIR spectra of IMS quasars from *Magellan*/FIRE and Gemini-N/GNIRS, smoothed to the instrumental resolution. The blue lines denote the errors of the spectra, and the red vertical lines indicate the locations of emission lines at the redshift determined from optical spectra. For the spectrum from Gemini-N/GNIRS, the gray bars show regions of strong atmospheric absorption.

IMS J0122+1216 ($z_{\text{Ly}\alpha} = 4.83$, $z_{\text{CIV}} = 4.81$). We classify this as a BAL quasar because of deep absorption features blueward of $\text{Ly}\alpha$, O I, Si IV+O IV], and C IV lines. It has a strong $\text{Ly}\alpha$ emission line, and a weak $\text{Ly}\beta$ emission line. We are not able to identify other emission lines due to these deep absorptions. The NIR spectrum has strong C IV, C III], and Mg II emission lines. The left side (shorter wavelengths) of these lines are severely absorbed. Yi et al. (2015) analyzed this quasar and derived a redshift of $z = 4.76$, whereas Wang et al. (2016) reported $z = 4.79$.

IMS J1437+0708 ($z_{\text{Ly}\alpha} = 4.94$). Its spectrum was obtained from NTT/EFOSC2 with $R \sim 130$, and it has the highest

S/N ratio among the optical spectra. However, it does not show any prominent emission lines except the $\text{Ly}\alpha$. Wang et al. (2016) reported $z = 4.93$.

IMS J2225+0330 ($z_{\text{Ly}\alpha} = 5.35$ and $z_{\text{Mg II}} = 5.26$). This source was observed by two telescopes—the KPNO 4 m telescope and NTT—and the two spectra were averaged together. It has a smooth $\text{Ly}\alpha$ emission line, but does not show any other emission lines. In the NIR spectrum, the C IV, C III], and Mg II emission lines are strong, but the C IV emission line has a rough shape due to the strong atmospheric absorption. Wang et al. (2016) reported $z = 5.24$.

IMS J1022+0801 ($z_{\text{Ly}\alpha} = 5.36$). This quasar has the weakest $\text{Ly}\alpha$ emission line among the six observed quasars. No other emission lines are visible, due to low S/N. This quasar was recently discovered independently by Yang et al. (2017), who report a spectroscopic redshift of $z = 5.30$.

IMS J0155+0415 ($z_{\text{Ly}\alpha} = 5.35$, $z_{\text{CIV}} = 5.27$). The optical spectrum shows a weak $\text{Ly}\alpha$ emission line, and other emission lines are not detected. In the NIR spectrum, it has prominent Si IV+O IV], C IV, and C III] emission lines. The Mg II emission line is hidden due to telluric absorption. Wang et al. (2016) reported $z = 5.37$.

4. Selection Completeness

To calculate the expected number of quasars for each selection method, we derived the quasar selection completeness, which can be affected by various effects. The completeness from color selection is defined as the fraction of quasars inside specific color cuts among all quasars within specific redshift and magnitude bins. First, applying various quasar templates, we calculated the completeness by means of taking the fraction of quasars that fall within each selection box as a function of redshift and M_{1450} (Section 4.1). We then apply this completeness to our quasar surveys and predict the expected quasar number of each selection method in Section 4.2.

4.1. Completeness from Color Cuts

To measure the likelihood that a quasar with a given redshift, M_{1450} , and intrinsic SED meets our selection criteria, we follow approaches from previous studies (e.g., Willott et al. 2005; Venemans et al. 2013). The composite quasar template from Vanden Berk et al. (2001) is redshifted to various values, assuming that the spectral properties of quasars do not evolve significantly with redshift (e.g., Kuhn et al. 2001; Fan et al. 2004; Jun et al. 2015), except wavelengths blueward of the $\text{Ly}\alpha$ line. Fluxes in these shorter wavelengths are absorbed by neutral hydrogen (H I) in the IGM, and the absorption becomes stronger toward higher redshift because the fraction of H I increases with redshift (Gunn–Peterson effect; Gunn & Peterson 1965). We applied this attenuation effect to our redshifted spectra using the IGM attenuation model of Madau et al. (1996). We redshifted the spectrum to $4 \leq z \leq 8$ with steps of $\Delta z = 0.05$, and adopted M_{1450} in the range $-30 < M_{1450} < -20$ with steps of $\Delta M_{1450} = 0.5$. We then calculated model magnitudes for each band.

The most important factor in the observed color distribution is the continuum slope of quasars. We considered 13 cases of models for each redshifted spectrum with continuum slopes of $-1.3 \leq \alpha_\nu \leq -0.1$ (where $F(\nu) \propto \nu^{\alpha_\nu}$) with steps of $\Delta \alpha_\nu = 0.1$. This range was derived based on the range of α_ν

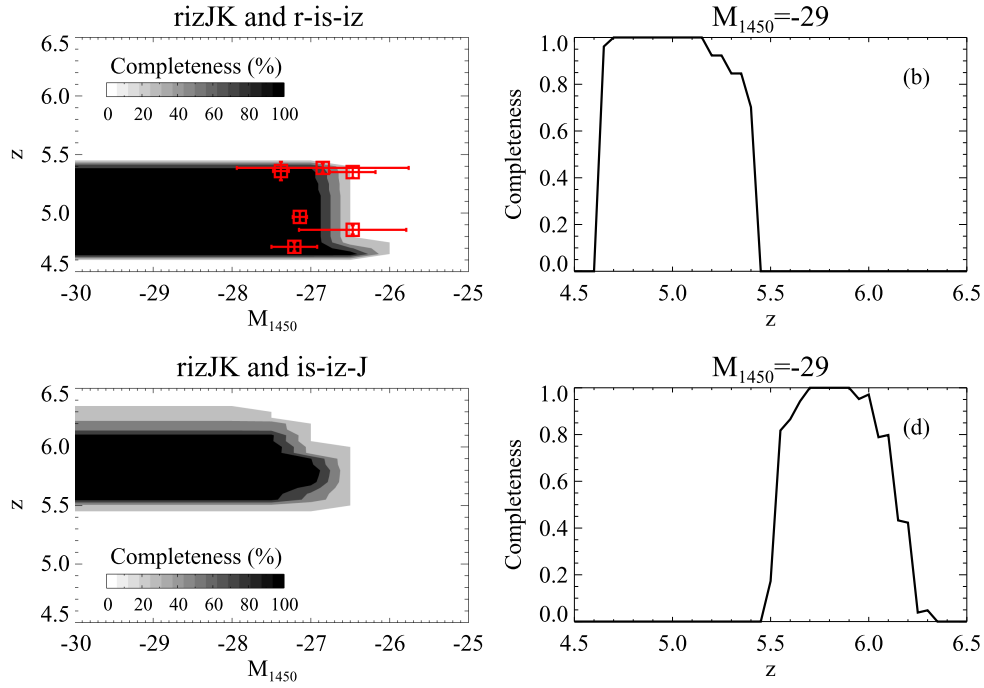


Figure 10. (a) Completeness as a function of redshift and M_{1450} for $r - i - z - J - K$ and $r - is - iz$ selection. The red boxes indicate the redshifts and M_{1450} of our six new quasars. (b) Completeness as a function of redshift from (a) when $M_{1450} = -29$. (c) Completeness for $r - i - z - J - K$ and $is - iz - J$ selection. (d) Completeness from (c) when $M_{1450} = -29$. The colors of the contours indicate 0% and 100% completeness for white and black, respectively.

values from the SDSS DR12 quasar catalog (Pâris et al. 2016) that includes about 230,000 quasars with a mean value of $\alpha_{\nu} = -0.7$ and a 1σ dispersion of 0.6 (68.3% confidence level). De Rosa et al. (2014) analyzed a sample of four quasars at $z > 6.5$, and three of them fall into this α_{ν} range. We also considered variable rest-frame equivalent widths (EW_0) of the Ly α emission line: eight cases of $50 \leq EW_0 \leq 85$ with steps of $\Delta EW_0 = 5$ (Fan et al. 2001). In total, we generate a database of 104 model quasars for which the continuum slopes and Ly α EWs are uniformly sampled within given ranges, and calculate the average selected fraction as a function of redshift and M_{1450} .

Figure 10(a) shows the completeness distribution as a function of redshift and M_{1450} , for the selection when using the $r - i - z - J - K$ and $r - is - iz$ color-color diagrams (selection method A). Figure 10(c) shows the completeness distribution when using $r - i - z - J - K$ and $is - iz - J$ color-color diagrams (selection method B). In Figures 10(b) and (d), we plot the completeness as a function of redshift for the two methods, for the case of $M_{1450} = -29$. The completeness in Figure 10(b) rises steeply from 0% to 100% between $z = 4.60$ and $z = 4.70$, remains at 100% up to $z = 5.15$, and drops below 80% for $z > 5.35$. In the case of Figure 10(d), the slopes of the completeness distribution at the borderline redshift values are more gradual than those in Figure 10(b). The redshift ranges of a completeness greater than 80% are $4.60 \leq z \leq 5.40$ for method A, and $5.50 \leq z \leq 6.05$ for method B. These represent the expected redshift ranges of quasars selected from the two color-color diagrams. The completeness of both selection methods drop to below 50% at $M_{1450} > -27.0$, when $z = 4.90$ and $z = 5.80$, and where the M_{1450} limit corresponds to our magnitude cut, $z < 19.5$ mag. We also plot the redshifts and M_{1450} of our six newly discovered quasars (Table 3) with red boxes in Figure 10(a).

4.2. Expected Quasar Number from Our Surveys

We calculated the expected number of quasars from our survey by extrapolating the luminosity function of $z \sim 6$ quasars from Willott et al. (2010b). We considered the 10^{kz} factor that accounts for the decline in number density as a function of redshift. We adopted two values of k : $k = -0.47$ from Willott et al. (2010b) and $k = -0.71$ from McGreer et al. (2013). We then extrapolated the luminosity function of $z \sim 6$ to our redshift range, and derived the expected number of quasars from our survey. Table 7 shows our quasar selection with different selection methods (column 1), survey areas (column 2), redshift ranges (column 3), and M_{1450} limits (column 4). The expected number of quasars for each quasar selection are listed in columns 5 and 6 for the cases of $k = -0.47$ and $k = -0.71$, respectively, with the 1σ errors caused by the uncertainties in break magnitude M_{1450}^* and bright end slope β from Willott et al. (2010b). We only considered the completeness from our color cuts, and assumed that 100% efficiency for each selection in its redshift range (column 3) and M_{1450} limit (column 5).

Our quasar survey discovered 20 quasars, including six new ones at $4.60 \leq z \leq 5.40$. This number is consistent with that from the luminosity function at $4.60 \leq z \leq 5.40$. However, we could not find any new quasars at $5.50 < z < 6.05$, except two previously discovered ones. We believe that the absence of any new quasars at $5.50 < z < 6.05$ is due to the lack of WISE photometry (they are fainter than quasars at $4.60 \leq z \leq 5.40$), resulting in a lower priority for the CQUEAN imaging. We expect to uncover more promising candidates as we build up the CQUEAN follow-up imaging sample.

5. Physical Properties of Quasars

In this section, we present the physical properties, based on the data obtained with optical and NIR spectroscopy, of four

Table 7
Expected Number of Quasars from Our Survey

Selection Method (1)	Area (deg ²) (2)	Redshift Range (3)	M_{1450} Limit (4)	Expected Number		Selected Number (7)
				(5) ^a	(6) ^b	
$r - is - iz$	3400	4.60–5.40	–27.0	$24.4^{+67.7}_{-17.9}$	$47.3^{131.2}_{-34.7}$	20
$is - iz - J$	3400	5.50–6.05	–27.0	$5.8^{+15.9}_{-4.3}$	$6.9^{+19.0}_{-5.1}$	2

Notes.^a For $k = -0.47$.^b For $k = -0.71$.

IMS quasars: IMS J0324+0426, IMS J0122+1216, IMS J2225+0330, and IMS J0155+0415. In our NIR spectra, we identified both the C IV and Mg II lines for IMS J0324+0426 and IMS J0122+1216, only the Mg II line for IMS J2225+0330, and only the C IV line for IMS J0155+0415. After modeling the continuum and emission lines of C IV and Mg II, we estimated continuum slopes α_ν (where α_ν is for $F(\nu) \propto \nu^{\alpha_\nu}$), line widths (full width at half maximum; FWHM), and continuum luminosities at the rest-frame wavelengths of 1350 Å and 3000 Å ($\lambda_{L_\lambda}(1350)$ and $\lambda_{L_\lambda}(3000)$) for each emission line (Section 5.1). From these measurements, we calculated the black hole mass (M_{BH}) from the C IV emission line ($M_{\text{BH,C IV}}$) or the Mg II emission line ($M_{\text{BH,Mg II}}$) through different relations from McLure & Jarvis (2004), Vestergaard & Peterson (2006), and Jun et al. (2015) (Section 5.2). For the virial factor in these black hole mass estimators, we adopted $f = 5.1 \pm 1.3$ from Woo et al. (2013). In Section 5.3, we compare the Eddington ratios of our quasars to lower-redshift quasars.

5.1. Analysis of NIR Spectra

We modeled the quasar NIR continuum assuming two components: a power-law component, and a component that describes the pseudo-continuum due to the blended forest of Fe II emission lines, as given below:

$$F(\lambda) = a \times \lambda^{\alpha_\lambda} + b \times \text{Fe II}(\lambda, \nu), \quad (1)$$

where α_λ is the continuum slope (in this case, $\alpha_\nu = -\alpha_\lambda - 2$ for $F(\lambda) \propto \lambda^{\alpha_\lambda}$), and ν and b are the width and strength of the Fe II templates. We used two Fe II templates from Vestergaard & Wilkes (2001) and Tsuzuki et al. (2006). A scaled and broadened Fe II template was used for modeling the Fe II emissions from our spectra. In the case of the C IV emission line, only Vestergaard & Wilkes (2001) provide the Fe II template in this wavelength range. We modeled the two components simultaneously.

The quality of the continuum subtraction depends on the determination of the continuum fitting ranges. We selected narrow fitting windows that minimize the contributions from other components. Because the qualities of the C IV emission line in the IMS J0324+0426 spectrum and the Mg II emission line in the IMS J2225+0330 spectrum are not sufficient to constrain the Fe II emissions, we failed to find the Fe II component. Because IMS J0122+1216 shows significant broad absorption features blueward of the C IV and Mg II emission lines, we narrowed the fitting window ranges to exclude the absorption part.

Because most of the uncertainties in the continuum slope or the line width result from the fitting range of the continuum modeling, we adopted 36 different fitting ranges within the given wavelength windows and performed model fitting for

each different sub-wavelength range to calculate the uncertainties. Since we cannot vary the continuum fitting range of C IV of IMS J0122+1216, we set the uncertainty of this line width as 5% of the line width instead of the uncertainty derived from the various continuum ranges. This fraction is identical to the ratio of line widths and their uncertainties, for all other lines.

After subtracting the best-fit continuum from each spectrum, we fit the C IV and Mg II emission lines. We used single and double-Gaussian profiles, considering the presence of asymmetric profiles characterized by red or blue wings. For the fitting ranges, we set 1500–1600 Å for the C IV line and 2700–2900 Å for the Mg II line, except for the C IV of IMS J0122+1216, which is affected by broad absorption. In that case, we set the fitting range to 1530–1590 Å. The Mg II lines of IMS J0324+0426 and IMS J0122+1216 are well-fit by double-Gaussian profiles, due to their asymmetric shapes, whereas the other lines can be fit using a single-Gaussian profile. One of the double-Gaussian components of IMS J0324+0426 is a narrow line (violet line in Figure 11(b)) with FWHM = $800 \pm 40 \text{ km s}^{-1}$. To obtain the line width FWHM, the measured FWHM_{obs} was corrected for the instrumental resolution FWHM_{ins}: $\text{FWHM} = \sqrt{(\text{FWHM}_{\text{obs}})^2 - (\text{FWHM}_{\text{ins}})^2}$.

We used an IDL procedure, `mpfit.pro`, to find the best-fit models to the observed spectra. It uses the χ^2 minimization method for both the continuum and the emission line. We included 1σ errors of the spectra for each fitting. From the best-fit model, we obtained the best-fit estimates for each parameter, such as the power-law slope and the line width. The uncertainties for each parameter were calculated as follows. The error for each parameter is dominated by the scatter of the various best-fits when altering the fitting range for the continuum. We compared the best-fit parameters for each trial, and set the average and standard deviation of the values as the best-fit parameter and its error.

5.2. Ultraviolet Luminosity and M_{BH}

In Figure 11, the best-fit continuum and emission line models are shown for each emission line. In Table 8, we list the best-fit estimates of the power law slope ($\alpha_{\nu,\text{C IV}}$ and $\alpha_{\nu,\text{Mg II}}$) and line width (FWHM_{C IV} and FWHM_{Mg II}), and their errors for each emission line. There is no significant difference in the derived power-law slope and line-width parameters when using different Fe II templates from Vestergaard & Wilkes (2001) and Tsuzuki et al. (2006). Note that the IMS 2225+0330 spectrum has low S/N, and the uncertainty of the line width estimated using the method in Section 5.1 could be underestimated (18%). On the other hand, the formal 1σ error from the Gaussian fitting is about 15%.

The power-law slopes of quasars vary significantly between sources. For example, Davis et al. (2007) found $-1.5 < \alpha_\nu < 0.5$

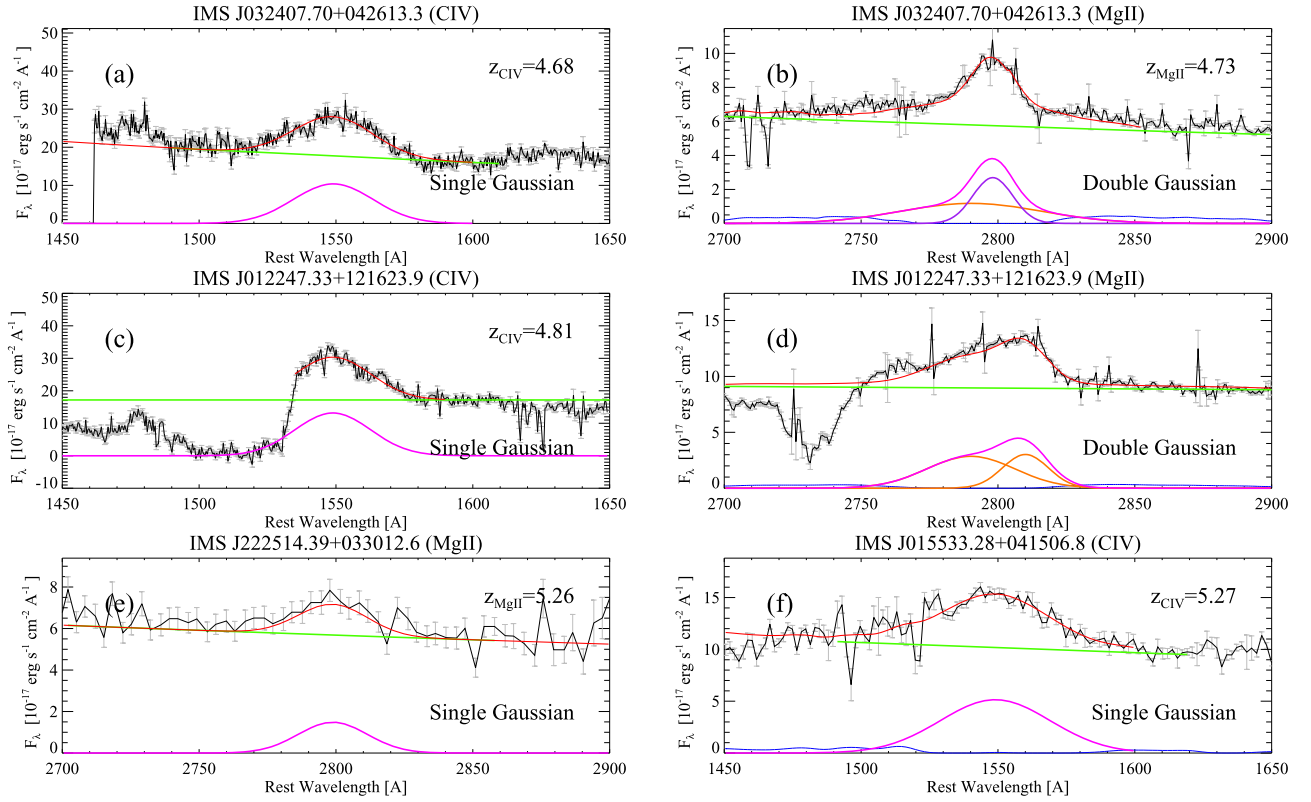


Figure 11. The best-fit continuum and emission line modeling for the C IV and Mg II emission lines of IMS quasars. In each panel, the spectrum (black) with errors (gray) is overplotted with the best-fit model (red), which consists of the power-law component (green), the best-fit Fe II template (blue; we used the Fe II template from Vestergaard & Wilkes 2001 as an example), and each emission line (magenta). Estimated redshift from each emission line is denoted, except for the Mg II emission line of IMS J0122+1216. (a) C IV emission line of IMS J0324+0426. We cannot find a solution for the Fe II template fitting. (b) Mg II emission line of IMS J0324+0426. We used a double-Gaussian model for the line fitting (violet and orange lines), and one of the double-Gaussian components is a narrow line (violet line). (c) C IV emission line of IMS J0122+1216. (d) Mg II emission line of IMS J0122+1216. Two Gaussian components (two orange lines) are used to fit the line shape. (e) Mg II emission line of IMS J2225+0330. We cannot find a solution for the Fe II template fitting. (f) C IV emission line of IMS J2225+0330.

Table 8
Power-law Slopes, Line Widths, and Continuum Luminosities Estimated from the NIR Spectra

Name	$\alpha_{\nu, \text{C IV}}$	$\alpha_{\nu, \text{Mg II}}$	$\text{FWHM}_{\text{C IV}}$ (km s^{-1})	$\text{FWHM}_{\text{Mg II}}$ (km s^{-1})	$\lambda L_{\lambda}(1350)$ ($10^{46} \text{ erg s}^{-1}$)	$\lambda L_{\lambda}(3000)$ ($10^{46} \text{ erg s}^{-1}$)
IMS J0324+0426	1.34 ± 0.60	-0.42 ± 0.78	6070 ± 300	2660 ± 280	6.93 ± 2.22	3.69 ± 0.35
IMS J0122+1216	...	-1.57 ± 0.31	6240 ± 310	4210 ± 160	5.91 ± 0.08	6.11 ± 0.64
IMS J2225+0330	...	0.49 ± 0.38	...	2750 ± 490	...	4.08 ± 0.22
IMS J0155+0415	-0.71 ± 0.85	...	8140 ± 800	...	6.44 ± 0.48	...

Table 9
 M_{BH} , L_{Bol} , L_{Edd} , and Eddington Ratios

Name	$M_{\text{BH, C IV}}$ ($10^9 M_{\odot}$)	$M_{\text{BH, Mg II}}$ ($10^9 M_{\odot}$)	$L_{\text{Bol}}(1350)$ ($10^{47} \text{ erg s}^{-1}$)	$L_{\text{Bol}}(3000)$ ($10^{47} \text{ erg s}^{-1}$)	$L_{\text{Edd}}(\text{C IV})$ ($10^{47} \text{ erg s}^{-1}$)	$L_{\text{Edd}}(\text{Mg II})$ ($10^{47} \text{ erg s}^{-1}$)	Edd. ratio (1350, C IV)	Edd. ratio (3000, Mg II)
IMS J0324+0426	7.60 ± 1.55	1.17 ± 0.31	2.6 ± 0.8	1.9 ± 0.2	9.6 ± 2.0	1.5 ± 0.4	0.28 ± 0.16	1.29 ± 0.60
IMS J0122+1216	7.38 ± 0.78	4.76 ± 0.52	2.3 ± 0.1	3.1 ± 0.3	9.3 ± 1.0	6.0 ± 0.7	0.24 ± 0.04	0.53 ± 0.16
IMS J2225+0330	...	1.35 ± 0.59	...	2.1 ± 0.1	...	1.7 ± 0.7	...	1.24 ± 0.91
IMS J0155+0415	13.53 ± 2.87	...	2.5 ± 0.2	...	17.1 ± 3.6	...	0.14 ± 0.05	...

for quasars at $0.76 < z < 1.26$ and $1.67 < z < 2.07$. At high redshift, quasars at $4 < z < 6.5$ from De Rosa et al. (2011) showed $-4 < \alpha_{\nu} < 0.7$, and quasars at $z > 6.5$ from De Rosa et al. (2014) showed $-0.67 < \alpha_{\nu} < 0.56$. The slope coefficients from our results are in agreement with these values at high redshift.

The $\lambda L_{\lambda}(1350)$ and $\lambda L_{\lambda}(3000)$ in Table 8 are also calculated from the optical and NIR spectra. For IMS J0324+0426, we used the optical and NIR spectra for the $\lambda L_{\lambda}(1350)$ and $\lambda L_{\lambda}(3000)$, respectively. The $\lambda L_{\lambda}(1350)$ of IMS J0155+0415 and the $\lambda L_{\lambda}(3000)$ of IMS J0122+1216 were estimated from

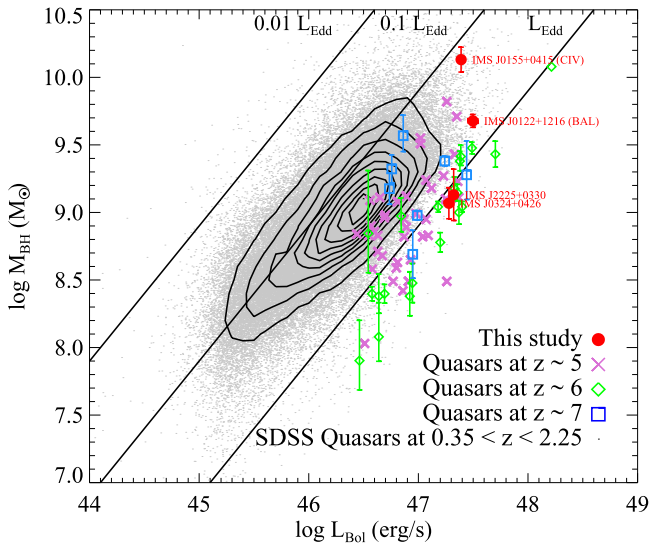


Figure 12. Here, we show M_{BH} as a function of L_{Bol} . Red filled circles are our sources, purple crosses are quasars at $z \sim 5$ (Trakhtenbrot et al. 2011), green diamonds are quasars at $z \sim 6$ (Jiang et al. 2007; Kurk et al. 2007, 2009; Wu et al. 2015), blue squares are quasars at $z \sim 7$ (De Rosa et al. 2014; Venemans et al. 2015), and gray points and black contours are a subsample of SDSS quasars at $0.35 < z < 2.25$ (Shen et al. 2011). Lines of constant Eddington ratio for $L_{\text{Bol}}/L_{\text{Edd}} = 0.01, 0.1, \text{ and } 1$ are plotted with black solid lines. The names of the four newly discovered quasars are written next to the red filled circles. Names with “BAL” and “CIV” are for the less reliable M_{BH} values (either a BAL quasar, or M_{BH} estimated from the C IV line.)

their NIR spectra. Because the continuum spectra near the 3000 Å of IMS J2225+0330 show low S/N due to the strong atmospheric absorption, we utilized fit spectra using the redshifted SDSS composite quasar template. In the case of the $\lambda L_{\lambda}(1350)$ of IMS J0122+1216, the continuum near 1350 Å shows deep drops in its optical spectrum. Therefore, we used the fit spectrum when we estimated the redshift in Section 3.2. The $\lambda L_{\lambda}(1350)$ and $\lambda L_{\lambda}(3000)$ were calculated from the average flux in the 1340–1360 Å and 2950–3050 Å, respectively. The uncertainty in the continuum luminosity was estimated from the scatter on the continuum flux in each window.

In Table 9, we list the virial black hole mass estimates obtained from C IV and Mg II emission lines ($M_{\text{BH,CIV}}$ and $M_{\text{BH,MgII}}$) by means of relations presented in Jun et al. (2015). The uncertainties of the masses propagate from the uncertainties of the FWHM and the continuum luminosity. The Eddington luminosities (L_{Edd}) estimated from the two mass estimators are listed in Table 9. Comparing the two mass estimates ($M_{\text{BH,CIV}}$ and $M_{\text{BH,MgII}}$) for IMS J0324+0426 and IMS J0122+1216, $M_{\text{BH,CIV}}$ is larger than $M_{\text{BH,MgII}}$ by 0.8 dex and 0.2 dex, respectively. We note that M_{BH} values from C IV show a larger scatter with respect to those from Mg II or $H\beta/H\alpha$ (e.g., Jun et al. 2015; Karouzos et al. 2015). For example, the intrinsic scatters of the $M_{\text{BH,CIV}}$ and $M_{\text{BH,MgII}}$ from Jun et al. (2015) is 0.40 dex and 0.09 dex, respectively. Therefore, the large discrepancy between $M_{\text{BH,CIV}}$ and $M_{\text{BH,MgII}}$ can be understood as a result of the large scatter in $M_{\text{BH,CIV}}$ estimators. Hence, we take the Mg II-based values to be more reliable. The M_{BH} values are roughly consistent with each other, when using different estimates (e.g., McLure & Jarvis 2004 or Vestergaard & Peterson 2006) that use the same emission line, within the error bars and the intrinsic scatter in the M_{BH} estimators.

5.3. Accretion Rate of Newly Discovered Quasars

Bolometric luminosities (L_{Bol}) and Eddington ratios are given in Table 9, where L_{Bol} are computed from $\lambda L_{\lambda}(1350)$ and $\lambda L_{\lambda}(3000)$ by multiplying them by 3.81 and 5.15, respectively (Shen et al. 2008).

For IMS J0122+1216, the L_{Bol} values that are calculated from $\lambda L_{\lambda}(1350)$ and $\lambda L_{\lambda}(3000)$ do not agree with each other. Because the $\lambda L_{\lambda}(1350)$ is estimated from the best-fit model spectrum, we adopt $\lambda L_{\lambda}(3000)$ as more reliable. In the case of IMS J0324+0426, the $L_{\text{Bol}}(1350)$ has a larger uncertainty due to significant contamination from sky emission lines.

The Eddington ratios from $M_{\text{BH,CIV}}$ and $\lambda L_{\lambda}(1350)$ are smaller by a factor of a few than those using $M_{\text{BH,MgII}}$ and $\lambda L_{\lambda}(3000)$. The discrepancy is most likely caused by the difference in the derived M_{BH} values. As we mentioned earlier, C IV-based M_{BH} values are generally less certain than Mg II-based values, and therefore we consider Mg II-based Eddington ratios to be more reliable.

Figure 12 shows M_{BH} as a function of L_{Bol} . To compare our sources with low-redshift quasars, we used the SDSS samples of quasars (Shen et al. 2011). Quasars with $M_{\text{BH,MgII}}$ information were selected, covering a redshift range of $0.35 < z < 2.25$ (gray points and black contours). We also include quasars at $z \sim 5$ (Trakhtenbrot et al. 2011, purple crosses), $z \sim 6$ (Jiang et al. 2007; Kurk et al. 2007, 2009; Wu et al. 2015, green empty diamonds), and $z \sim 7$ (De Rosa et al. 2014; Venemans et al. 2015, blue empty squares). All M_{BH} values are derived using Mg II estimators. The Eddington ratios, $L_{\text{Bol}}/L_{\text{Edd}} = 0.01, 0.1, \text{ and } 1$, are indicated with black solid lines. Our sources are plotted with the red filled circles from $M_{\text{BH,MgII}}$ and $L_{\text{Bol}}(3000)$, except IMS J0155+0415. We can see that the high-redshift sample occupies a region of the parameter space different from that of the low-redshift sample with similar L_{Bol} : the Eddington ratios of these high-redshift quasars are significantly larger than those of the low-redshift sample. In particular, our high-redshift quasars have Eddington ratios around 1, suggesting that these quasars are growing vigorously. The Eddington ratio of IMS J0155+0415 is an exception, because it was estimated from $M_{\text{BH,CIV}}$ and $L_{\text{Bol}}(1350)$, which are less reliable than $M_{\text{BH,MgII}}$ and $L_{\text{Bol}}(3000)$, respectively. Willott et al. (2010a) show similar results, where the luminosity-matched quasar samples at $z = 2$ and $z = 6$ have different Eddington ratio distributions. However, to compare the Eddington ratio distribution of low-redshift quasars to their high-redshift counterparts, less luminous samples will be needed. Intrinsic Eddington ratios of normal high-redshift quasars can be studied by discovering quasars from deeper surveys (e.g., Kashikawa et al. 2015; Kim et al. 2015) and Eddington ratio distributions at high redshift when less luminous quasars are included can be different (e.g., Y. Kim et al. 2017, in preparation).

6. Summary

We conducted a quasar survey at $5 \lesssim z \lesssim 5.7$ using multi-wavelength data with new selection techniques. First, candidates were selected from our $r - i - z - K$ color cuts, then we exploited the WISE colors to narrow down the candidates. The candidates were also observed with the CQUEAN is and iz filters, which overcome the limitations of previous filter systems. We then carried out optical spectroscopic observations to confirm our high-redshift quasar

candidates and discovered six new quasars. Four of them were observed by NIR spectroscopy to measure their physical properties (M_{BH} , L_{Bol} , L_{Edd} , and Eddington ratio) via spectral modeling of their continuum and emission lines. We compared Eddington ratios of our sources to those of low- and high-redshift quasars, and found that the Eddington ratio of our quasars at $z \sim 5$ have values close to 1. These results, characterized by high luminosities ($M_{1450} < -27$ mag), larger black hole masses of $>10^9 M_{\odot}$, and near-Eddington limit luminosities, support the scenario of rapid growth of SMBHs in the early universe.

This work was supported by the National Research Foundation of Korea (NRF) grant, No. 2008–0060544, funded by the Korean government (MSIP). The Gemini data were taken through the K-GMT Science Program (PID: KR-2015B-005) of Korea Astronomy and Space Science Institute (KASI). Based on observations obtained at the Gemini Observatory, acquired through the Gemini Observatory Archive, and processed using the Gemini IRAF package, which is operated by the Association of Universities for Research in Astronomy, Inc., under a cooperative agreement with the NSF on behalf of the Gemini partnership: the National Science Foundation (United States); the National Research Council (Canada); CONICYT (Chile); Ministerio de Ciencia, Tecnología, e Innovación Productiva (Argentina); and Ministério da Ciência, Tecnologia, e Inovação (Brazil). This paper includes data taken at The McDonald Observatory of The University of Texas at Austin. Based on observations at Kitt Peak National Observatory, National Optical Astronomy Observatory (NOAO Prop. ID: 2012B-0537, 2013A-0506, 2013B-0534; PI: Y. Jeon), which is operated by the Association of Universities for Research in Astronomy (AURA), under cooperative agreement with the National Science Foundation, the authors are honored to be permitted to conduct astronomical research on Iolkam Du'ag (Kitt Peak), a mountain with particular significance to the Tohono O'odham. This paper includes data gathered with the 6.5 meter *Magellan* Telescopes located at Las Campanas Observatory, Chile. M.H. acknowledges the support from Global Ph.D. Fellowship Program, through the National Research Foundation of Korea (NRF), funded by the Ministry of Education (NRF-2013H1A2A 1033110). H.D.J. is supported by an appointment to the NASA Postdoctoral Program at the Jet Propulsion Laboratory, administered by Universities Space Research Association under contract with NASA, and by the Basic Science Research Program through the NRF funded by the Ministry of Education (NRF-2017R1A6A3A04005158). D.K. acknowledges fellowship support from the grant NRF-2015-Fostering Core Leaders of Future Program, No. 2015-000714 funded by the Korean government. We thank the anonymous referee for useful comments, which improved the content of this paper.

Facilities: Mayall (RCSPL), NTT (EFOSC2), *Magellan*: Baade (FIRE), Gemini:North (GNIRS).

ORCID iDs

Yiseul Jeon  <https://orcid.org/0000-0003-4847-7492>
 Myungshin Im  <https://orcid.org/0000-0002-8537-6714>
 Yongjung Kim  <https://orcid.org/0000-0003-1647-3286>
 Hyunsung David Jun  <https://orcid.org/0000-0003-1470-5901>
 Soojong Pak  <https://orcid.org/0000-0002-2548-238X>
 Marios Karouzos  <https://orcid.org/0000-0002-8858-3188>

Duho Kim  <https://orcid.org/0000-0001-5120-0158>
 Ji Hoon Kim  <https://orcid.org/0000-0002-1418-3309>
 Minjin Kim  <https://orcid.org/0000-0002-3560-0781>
 Seong-Kook Lee  <https://orcid.org/0000-0001-5342-8906>

References

- Bañados, E., Venemans, B. P., Decarli, R., et al. 2016, arXiv:1608.03279
 Bañados, E., Venemans, B. P., Morganson, E., et al. 2014, *AJ*, 148, 14
 Bertin, E. 2006, *adass XV*, 351, 112
 Bertin, E., & Arnouts, S. 1996, *A&AS*, 117, 393
 Bruzual, G., & Charlot, S. 2003, *MNRAS*, 344, 1000
 Burrows, A., Sudarsky, D., & Hubeny, I. 2006, *ApJ*, 640, 1063
 Buzzoni, B., Delabre, B., Dekker, H., et al. 1984, *Msngr*, 38, 9
 Cardelli, J. A., Clayton, G. C., & Mathis, J. S. 1989, *ApJ*, 345, 245
 Cool, R. J., Kochanek, C. S., Eisenstein, D. J., et al. 2006, *AJ*, 132, 823
 Davis, S. W., Woo, J.-H., & Blaes, O. M. 2007, *ApJ*, 668, 682
 De Rosa, G., Decarli, R., Walter, F., et al. 2011, *ApJ*, 739, 56
 De Rosa, G., Venemans, B. P., Decarli, R., et al. 2014, *ApJ*, 790, 145
 Fan, X., Hennawi, J. F., Richards, G. T., et al. 2004, *AJ*, 128, 515
 Fan, X., Narayanan, V. K., Lupton, R. H., et al. 2001, *AJ*, 122, 2833
 Fan, X., Strauss, M. A., Richards, G. T., et al. 2006, *AJ*, 131, 1203
 Fan, X., Strauss, M. A., Schneider, D. P., et al. 1999, *AJ*, 118, 1
 Fan, X., Strauss, M. A., Schneider, D. P., et al. 2003, *AJ*, 125, 1649
 Gunn, J. E., & Peterson, B. A. 1965, *ApJ*, 142, 1633
 Gunn, J. E., & Stryker, L. L. 1983, *ApJS*, 52, 121
 Hewett, P. C., Warren, S. J., Leggett, S. K., & Hodgkin, S. T. 2006, *MNRAS*, 367, 454
 Ikeda, H., Nagao, T., Matsuoka, K., et al. 2012, *ApJ*, 756, 160
 Im, M. 2009, in ASP Conf. Ser. 418, AKARI, a Light to Illuminate the Misty Universe, ed. T. Onaka et al. (San Francisco, CA: ASP), 227
 Im, M., Griffiths, R. E., & Ratnatunga, K. U. 1997, *ApJ*, 475, 457
 Jeon, Y., Im, M., Pak, S., et al. 2016, *JKAS*, 49, 25
 Jiang, L., Fan, X., Annis, J., et al. 2008, *AJ*, 135, 1057
 Jiang, L., Fan, X., Bian, F., et al. 2009, *ApJL*, 138, 305
 Jiang, L., Fan, X., Brandt, W. N., et al. 2010, *Natur*, 464, 380
 Jiang, L., Fan, X., Vestergaard, M., et al. 2007, *AJ*, 134, 1150
 Jiang, L., McGreer, I. D., Fan, X., et al. 2015, *AJ*, 149, 188
 Jun, H. D., Im, M., Lee, H. M., et al. 2015, *ApJ*, 806, 109
 Karouzos, M., Woo, J.-H., Matsuoka, K., et al. 2015, *ApJ*, 815, 128
 Kashikawa, N., Ishizaki, Y., Willott, C. J., et al. 2015, *ApJ*, 798, 28
 Kim, E., Park, W.-K., Jeong, H., et al. 2011, *JKAS*, 44, 115
 Kim, Y., Im, M., Jeon, Y., et al. 2015, *ApJL*, 138, L35
 Kuhn, O., Elvis, M., Bechtold, J., & Elston, R. 2001, *ApJS*, 136, 225
 Kurk, J. D., Walter, F., Fan, X., et al. 2007, *ApJ*, 669, 32
 Kurk, J. D., Walter, F., Fan, X., et al. 2009, *ApJ*, 702, 833
 Laor, A., & Davis, S. W. 2011, *MNRAS*, 417, 681
 Lawrence, A., Warren, S. J., Almaini, O., et al. 2007, *MNRAS*, 379, 1599
 Leipski, C., Meisenheimer, K., Walter, F., et al. 2014, *ApJ*, 785, 154
 Lim, J., Chang, S., Pak, S., et al. 2013, *JKAS*, 46, 161
 Madau, P., Ferguson, H. C., Dickinson, M. E., et al. 1996, *MNRAS*, 283, 1388
 Mahabal, A., Stern, D., Bogosavljević, M., Djorgovski, S. G., & Thompson, D. 2005, *ApJL*, 634, L9
 Matute, I., Masegosa, J., Márquez, I., et al. 2013, *A&A*, 557, A78
 McGreer, I. D., Jiang, L., Fan, X., et al. 2013, *ApJ*, 768, 105
 McLure, R. J., & Jarvis, M. J. 2004, *MNRAS*, 353, L45
 Mortlock, D. J., Patel, M., Warren, S. J., et al. 2009, *A&A*, 505, 97
 Mortlock, D. J., Warren, S. J., Venemans, B. P., et al. 2011, *Natur*, 474, 616
 Pâris, I., Petitjean, P., Ross, N. P., et al. 2016, arXiv:1608.06483
 Park, W.-K., Pak, S., Im, M., et al. 2012, *PASP*, 124, 839
 Patten, B. M., Stauffer, J. R., Burrows, A., et al. 2006, *ApJ*, 651, 502
 Polsterer, K. L., Zinn, P.-C., & Gieseke, F. 2013, *MNRAS*, 428, 226
 Richards, G. T., Myers, A. D., Gray, A. G., et al. 2009, *ApJS*, 180, 67
 Richards, G. T., Myers, A. D., Peters, C. M., et al. 2015, arXiv:1507.07788
 Schlegel, D. J., Finkbeiner, D. P., & Davis, M. 1998, *ApJ*, 500, 525
 Schneider, D. P., Fan, X., Strauss, M. A., et al. 2001, *AJ*, 121, 1232
 Sharp, R. G., McMahon, R. G., Irwin, M. J., & Hodgkin, S. T. 2001, *MNRAS*, 326, L45
 Shen, Y., Greene, J. E., Strauss, M. A., Richards, G. T., & Schneider, D. P. 2008, *ApJ*, 680, 169
 Shen, Y., Richards, G. T., Strauss, M. A., et al. 2011, *ApJS*, 194, 45
 Trakhtenbrot, B., Netzer, H., Lira, P., & Shemmer, O. 2011, *ApJ*, 730, 7
 Tsuzuki, Y., Kawara, K., Yoshii, Y., et al. 2006, *ApJ*, 650, 57
 Vanden Berk, D. E., Richards, G. T., Bauer, A., et al. 2001, *AJ*, 122, 549

- Venemans, B. P., Bañados, E., Decarli, R., et al. 2015, [ApJL](#), **801**, L11
- Venemans, B. P., Findlay, J. R., Sutherland, W. J., et al. 2013, [ApJ](#), **779**, 24
- Vestergaard, M., & Peterson, B. M. 2006, [ApJ](#), **641**, 689
- Vestergaard, M., & Wilkes, B. J. 2001, [ApJS](#), **134**, 1
- Wang, F., Wu, X.-B., Fan, X., et al. 2016, [ApJ](#), **819**, 24
- Wang, J.-M., Du, P., Li, Y.-R., et al. 2014, [ApJL](#), **792**, L13
- Willott, C. J., Albert, L., Arzoumanian, D., et al. 2010a, [AJ](#), **140**, 546
- Willott, C. J., Delfosse, X., Forveille, T., Delorme, P., & Gwyn, S. D. J. 2005, [ApJ](#), **633**, 630
- Willott, C. J., Delorme, P., Omont, A., et al. 2007, [AJ](#), **134**, 2435
- Willott, C. J., Delorme, P., Reylé, C., et al. 2009, [AJ](#), **137**, 3541
- Willott, C. J., Delorme, P., Reylé, C., et al. 2010b, [AJ](#), **139**, 906
- Woo, J.-H., Schulze, A., Park, D., et al. 2013, [ApJ](#), **772**, 49
- Wu, X.-B., & Jia, Z. 2010, [MNRAS](#), **406**, 1583
- Wu, X.-B., Wang, F., Fan, X., et al. 2015, [Natur](#), **518**, 512
- Yang, J., Fan, X., Wu, X.-B., et al. 2017, [AJ](#), **153**, 184
- Yang, J., Wang, F., Wu, X.-B., et al. 2016, [ApJ](#), **829**, 33
- Yi, W., Wu, X., Wang, F., et al. 2015, [SCPMA](#), **58**, 5685
- Zhang, Z. H., Pokorny, R. S., Jones, H. R. A., et al. 2009, [A&A](#), **497**, 619
- Zheng, W., Tsvetanov, Z. I., Schneider, D. P., et al. 2000, [AJ](#), **120**, 1607